Multicore fibre-based clock synchronisation for ultra-low latency data centre interconnections

Miguel Antonio Chavez Tapia

Centre of Doctoral Training

Registered student at

University of Cambridge

MRes in Integrated Photonic and Electronic Systems

Supervisor: Dr Zhixin Liu, 2017/2018

I hereby declare that, except where specifically indicated, the work submitted herein is my own original work.

Miguel Antonio Chavez Tapia

Abstract

The information technology market evolution towards cloud services and the undeniable growth of data traffic have triggered the conception of the hyper-scale data centres. Intrinsically, cloud services require capability to cope with the high data traffic to serve the customers and required internal processes for high quality services.

Optical technologies have enabled to handle higher the data traffic and multi-core fibre’s capacity for high data rate transmission comes as a promising solution for data centre interconnections, enabling clock signal transmission parallel to data transmission, thus increasing performance by reducing clock synchronization overhead and time for clock recovery.

However, in a data centre, while the environmental variables are controlled, it operates in a variable range, thus these variations need to be accounted. In this study, the effects of the temperature on the inter-core skew variation, of a multi-core fibre, are measured and analysed. The experimental setup, which uses an interferometer to measure the relative delay differences in a pair of cores, is a novel approach for inter-core skew variation quantification. Moreover, using this technique, the achieved resolution is in the order of femtoseconds.

The results show an increase in inter-core skew variation between a pair of cores proportional to the increase in temperature. Additionally, adjacent cores demonstrate the lowest variation.

Acknowledgements

I wish to express my profound gratitude to my supervisor, Dr Zhixin Liu, who was eager to share uncountable hours discussing the topics required for the culmination of this project, from the most basic theory, through the elemental laboratory training and the findings of this project.

Additionally, my gratitude to all the people in the Optical Networks Group in UCL, to Kari, Petros, Hui, Paris, Joshua, and all the talented researchers and students.

I also want to thank two people from the University of Cambridge, Division B: Prof. Richard Penty and Ms. Victoria Barret for the constant support.

Contents

List of tables

List of figures

List of acronyms

IT	Information technology
PC	Personal computer
VPN	Virtual private network
SMTP	Simple mail transfer protocol
PTP	Precision time protocol
DTP	Data centre time protocol
NTP	Network time protocol
MCF	Multi-core fibre
SMF	Single-mode fibre
OH-	Hydroxide ion
SDM	Spatial-division multiplexing
FMF	Few-mode fibre
MC-FMF	Multi-core few-mode fibre}
WDM	Wavelength-division multiplexing
SC-SMF	Single-core single-mode fibre
MEF	Multi-element fibre
SM-MCF	Single-mode multi-core fibre
ICXT	Inter-core crosstalk
MFD	Mode-field diameter
IC-skew	Inter-core skew
SSC	Spatial super-channel
DSP	Digital signal processing
TCD	Thermal coefficient delay
PSOF	Phase stabilised optical fibre
HC-PBGF	Hollow-core photonic bandgap fibre
PBG	Photonic bandgap
PPG	Pulse pattern-generator
OOK	On-off keying

PRBS	Pseudo-random binary sequence
EDFA	Erbium-doped fibre amplifier
BPF	Bandpass filter
NRZ	No-return-zero
VOA	Variable optical attenuator
PD	Photodetector
CW	Constant wave
RIN	Relative intensity noise
CSV	Comma-separated value

Chapter 1.

Introduction

1.1 Cloud services evolution

The birth of cloud computing can be traced to the Compaq Computer offices in 1996. Its executives envisioned web services and applications running on the cloud, which was a metaphor for the internet [1]. Even though the term was not popular in the IT industry until 2006, companies such as Amazon, Microsoft, Google, IBM, and others already offered cloud computing services. The growth in the demand for these services continues to push the limits of the technology that underpins cloud services and expands the information technology (IT) market.

Cloud computing can be defined as follows: “a set of network-enabled services, providing scalable, QoS guaranteed, normally personalized, inexpensive computing infrastructures on demand, which could be accessed in a simple and pervasive way” [2]. The principal value that cloud services add is to remove the IT management from the business they serve, effectively reducing the time spent on it.

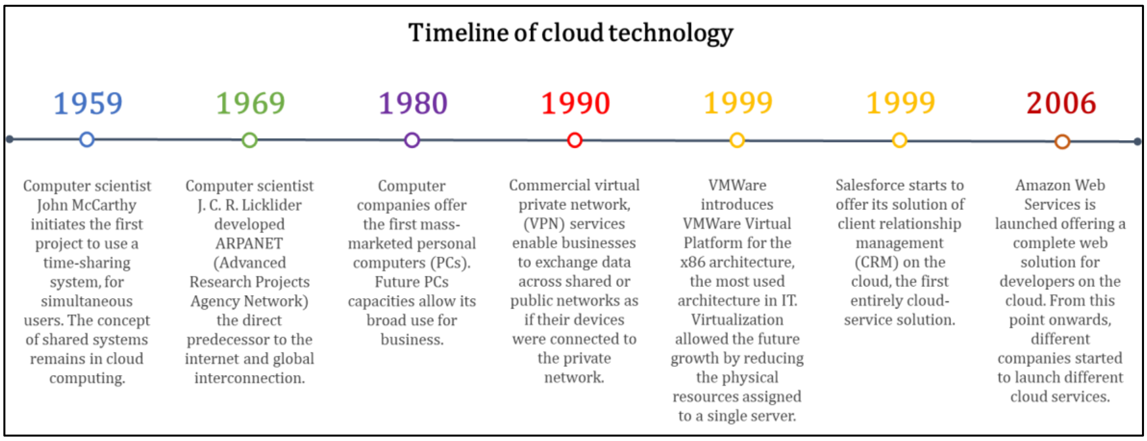

1959: Computer scientist John McCarthy initiates the first project to use a time-sharing system, for simultaneous users. The concept of shared systems remains in cloud computing.

1969: Computer scientist J. C. R. Licklider developed ARPANET (Advanced Research Projects Agency Network) the direct predecessor to the internet and global interconnection.

1980: Computer companies offer the first mass-marketed personal computers (PCs). Future PCs capacities allow its broad use for business.

1990: Commercial virtual private network, (VPN) services enable businesses to exchange data across shared or public networks as if their devices were connected to the private network.

1999: VMWare introduces VMWare Virtual Platform for the x86 architecture, the most used architecture in IT. Virtualization allowed the future growth by reducing the physical resources assigned to a single server.

1999: Salesforce starts to offer its solution of client relationship management (CRM) on the cloud, the first entirely cloud-service solution.

2006: Amazon Web Services is launched offering a complete web solution for developers on the cloud. From this point onwards, different companies started to launch different cloud services.

Figure 1.1. Timeline of cloud technology, modified from [3]

The evolution of cloud services was possible due to some technology developments. Figure 1.1 utilises a timeline to depict the key technologies and businesses which helped shape the current cloud solutions. One essential concept of cloud computing is a shared system which goes back to 1959. The Internet and the personal computer (PC) helped define the host-server architecture: a *server* is a computing device which performs service to queries from many *host* computing devices. Technologies like virtual private network (VPN) and virtualisation were key in the timeline of cloud computing. The next step was the birth of the firsts cloud services, like Salesforce or Amazon Web Services.

In the traditional computing services solution, called on-premise, the business owns and manages the IT infrastructure. Figure 1.2 shows a client-server architecture for both on-premise and cloud solutions for an email service: a client's device requests a connection to the simple mail transfer protocol (SMTP) port 25 on the email server. Another goal of cloud services is to provide the same quality as if the service were running on-premise (i.e., timely service response, high-availability, auditing, among other requirements) which are part of the service agreement.

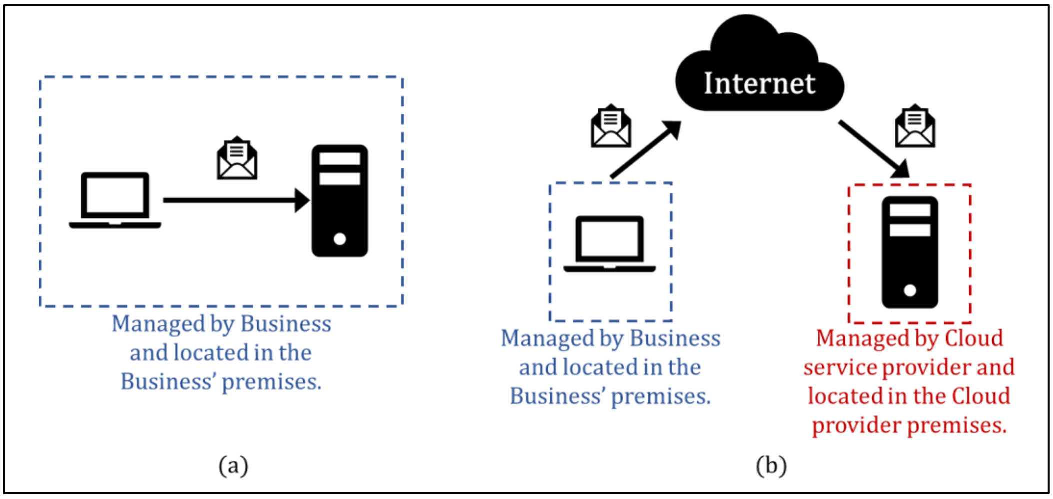

Figure 1.2. Client-server email service architecture for (a) on-premise service and (b) cloud service

A direct consequence of the adoption of cloud services is the increase of the data centre of the cloud service provider. This is easily inferred from Figure 1.2, as the server capacities are moved from the business' premises to the cloud provider's premises. Moreover, according to a survey, 83% of enterprises' workload will be serviced by a cloud solution by 2020 [4], which means larger data centres for the cloud providers.

1.2 Hyper-scale data centres

The increase in the IT demand and the arrival of cloud services also triggered the growth of the data centres, which host these services. A data centre is a building where multiple servers and communication devices are co-located because of their common requirements, like environmental, energy, security among others [5]. Generally, an hyper-scale data centre hosts hundreds of thousands of servers and is larger than a hundred thousand feet square [6].

According to Cisco's report, by 2021, the number of hyper-scale data centres will grow to 628 and the annual global cloud traffic will reach 1.6ZB per month [7]. Figure 1.3 demonstrates this growth trend. As an example of Google's data centre network, the bandwidth demands are increasing more than twice every year and more than 1Pbps of bisection bandwidth [8], which goes along with the better performance of the processing devices. Therefore, there is a need for high-performance and low latency links inside of the data centre, along with reliability and high-availability.

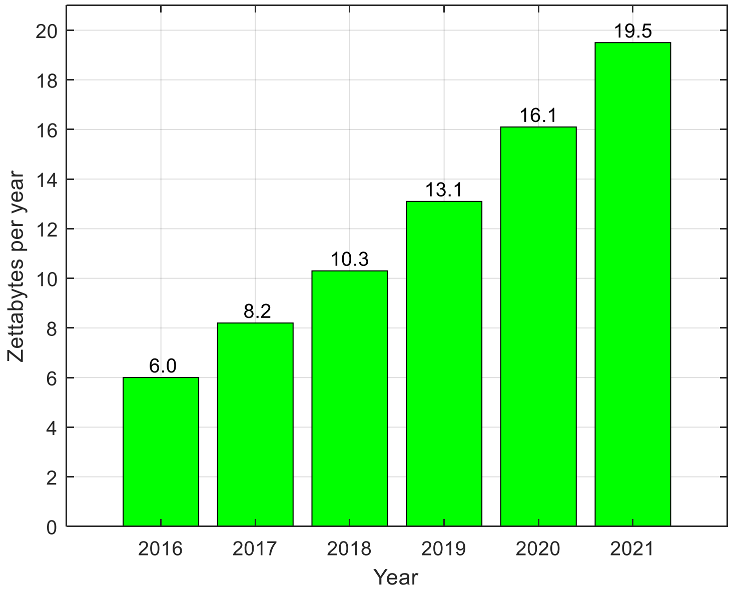

Figure 1.3. Cloud data centre traffic growth [7]

1.3 Data centre interconnection technologies

Hyper-scale data centres are based on the Clos topology [9], which is network architecture which uses stages of electronic switches and provides fault tolerance, path diversity, scalability and high bandwidth [8]. Figure 1.4 shows an example of this topology. However, for large networks, the main drawbacks are the cabling complexity and the cost necessary to provide full bandwidth between its extreme points [10] [11]. The final bandwidth limitation is in the electronic switch. As mentioned in [9], the Clos topology can alleviate the bandwidth impairment but, as the electronic switch reaches its limits, a new approach becomes necessary. There are proposals to use optical switches for data centre networking, thus increasing bandwidth and reducing electrical power consumption.

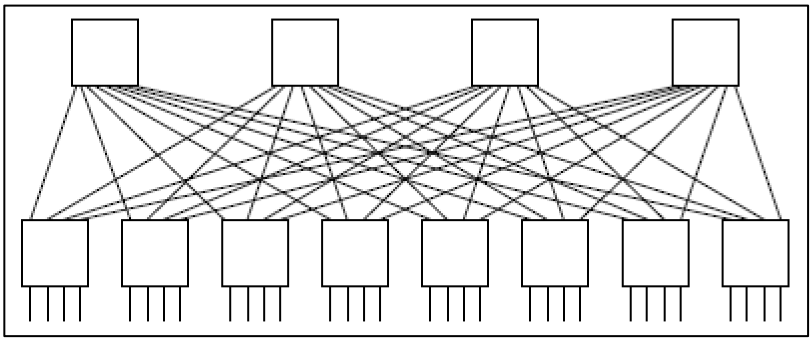

Figure 1.4. Folded Clos Network with 2 levels and radix 8, switches with 8 ports [11]

1.4 Clock synchronisation

Conveying a clock signal to the servers in a hyper-scale data centre is crucial. Synchronisation among devices determines lower congestion in data centre networks and improves network updates and synchronous data stream [12], which are used in the replication of high availability solutions, which is an essential tool for cloud services.

Further improvements in this field have developed as newer protocols such as precision time protocol (PTP) or data centre time protocol (DPT) over the traditional network time protocol (NTP) [13] demonstrate the importance of clock distribution. Some of the restrictions of these protocols include the addition of an overhead for clock synchronisation, for instance in PTP, or the addition of specific hardware, for instance in DTP, and extra processing time for clock recovery.

However, a new approach is the use of multi-core fibre (MCF) which allows multiple transmission channels. To improve the performance, a clock signal can be distributed along one of its cores while transmitting data signals in the other ones. This approach significantly reduces the drawback of the additional overhead and the processing for clock recovery, as all the devices receive the clock signal.

1.5 Scope of the report

The work presented in this section outlines a trend towards an increase in data traffic, cloud services and the data centres where these services are hosted. Therefore, the speed of data and clock transmission requires improvement in order to provide higher quality services. MCF has been proposed as a solution to data centre interconnection for the transmission of data and clock signals. MCF has multiple cores which allow parallel optical transmission channels.

Within a data centre, due to the operation requirement of the computing and communication devices, the temperature must be controlled. However, the temperature profile is not uniform, as there are cold and hot aisles. Figure 1.5 depicts this profile, which basically works by cooling air in the cold aisle, with the computing and communication devices using this airflow for cooling, and then releasing hot air into the hot aisle. Moreover, the temperature profile is also time-dependent, as it is proportional to the power consumption of the same devices, which is proportional to their workload at a particular moment.

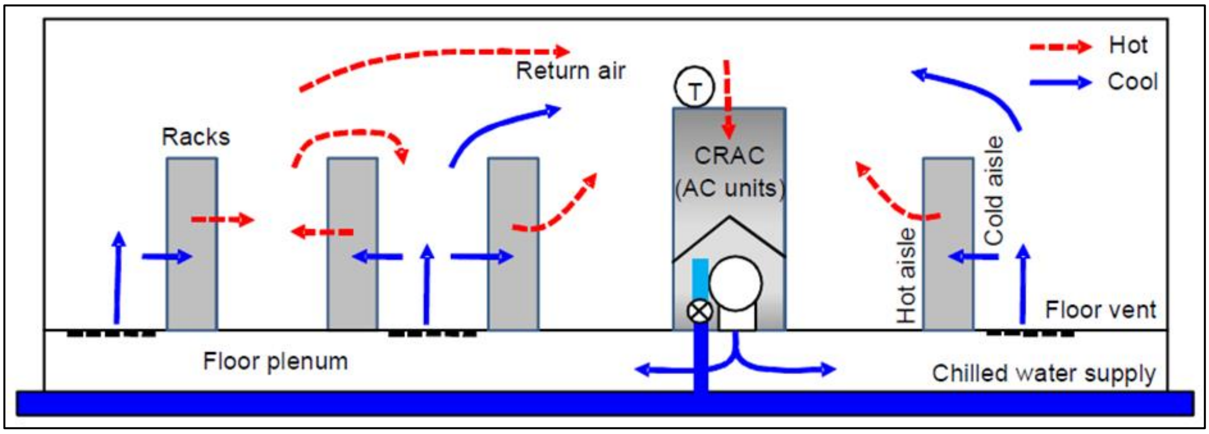

Figure 1.5. An illustration of an air-cooled data centre [14]

This report focuses on analysing the effect of temperature change in the transmission of signals through an MCF and on performing an experimental measurement of this effect. More specifically, this report investigates the time delay variation between different cores in MCF and its dependence on temperature. Overall, this experimental measurement aims to replicate worst-case scenarios of a data centre environment.

Chapter 2.

Multi-core optical fibre

The telecommunications industry growth was and still is underpinned by the development of the optical fibre. The main advantages are its low loss profile for high distances and its broad bandwidth. The MCF is a promising solution for capacity increase.

2.1 The optical fibre as a waveguide

In any material, light propagates at a velocity defined by equation *2.1*, where n is the material refractive index and c the speed of light.

$$v = \frac{c}{n} \qquad (2.1)$$

An optical fibre works by guiding light inside of its cylindrical dielectric core due to the difference between the refractive indexes of the core and the cladding, n_1 and n_2, as shown in Figure 2.1. Equation 2.2 derives from applying Snell's Law in the air-core boundary. The light is then propagated inside of the core with a different angle until it reaches the core-cladding boundary. Considering $n_1 > n_2$, the limit value of the angle ϕ'_r is 90 degrees, as only light with an angle higher than this value is guided. This defines the critical angle of ϕ presented in equation 2.3.

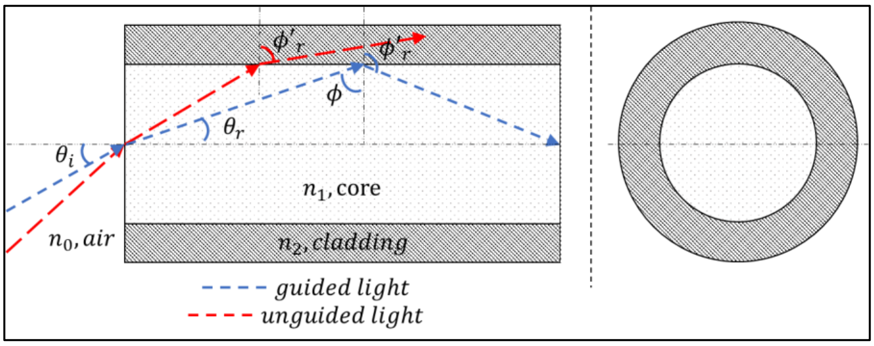

Figure 2.1. An optical fibre: a cylindrical core and cladding

$$n_0 \sin \theta_i = n_1 \sin \theta_r \qquad (2.2)$$

$$\sin \phi_c = \frac{n_2}{n_1} \qquad (2.3)$$

Figure 2.1 also demonstrates that the cosine of ϕ is equal to the sine of θ_r. Using equation 2.3 to calculate the cosine of ϕ_c, the numerical aperture derives from solving equation 2.2, which is presented in equation 2.4. The numerical aperture value is a representation of the core's capacity to gather light.

$$N.A. = n_0 \sin\theta_i = \sqrt{{n_1}^2 - {n_2}^2} \qquad (2.4)$$

2.2 Characteristics of the optical fibre

2.2.1 Mode propagation

The optical fibre core diameter and the refractive index of the core and the cladding define the number of guided modes that are propagated in an optical fibre. Using Maxwell's equation, the propagation of light as a field is described as a wave equation, presented in equation *2.5*, where $\tilde{E}$ is the optical field, n is the refractive index and k_0 is the free-space wavenumber.

$$\nabla^2\tilde{E} + n^2 k_0 \tilde{E} = 0 \qquad (2.5)$$

The solutions to this equation are the optical modes which satisfy the boundaries conditions and have a constant spatial distribution with propagation [15]. A typical value of core diameter of 9µm defines a single-mode fibre, which allows the propagation of only one mode, and of 62.5µm, which allows the propagation of multiple modes. The difference between the propagation in these optical fibres is presented in Figure 2.2.

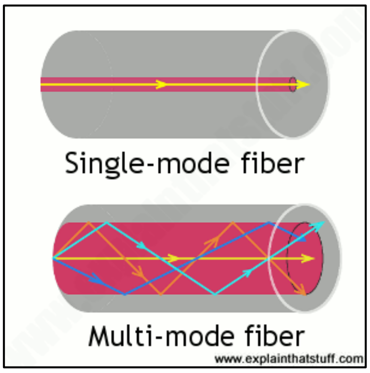

Figure 2.2. Mode propagation in optical fibres [16]

Equation *2.1* portrays the light velocity in a material. However, a narrow-band optical pulse travels at a different velocity, the group velocity, v_g. Using the group refractive index, n_g, in the same equation gives the value of v_g. The time it takes for a pulse to travel at the group velocity for a fibre length is the propagation delay.

2.2.2 Dispersion in optical fibre

A limitation of the light propagation in an optical fibre is the temporal broadening of the light pulses, which is known as dispersion, shown in Figure 2.3. Dispersion limits the achievable bandwidth for a fibre length. Thus, it is one factor that defines the maximum length and the repeaters required for a certain distance. The usual unit of dispersion is ps/nm-km to express the time broadening per optical wavelength and fibre distance.

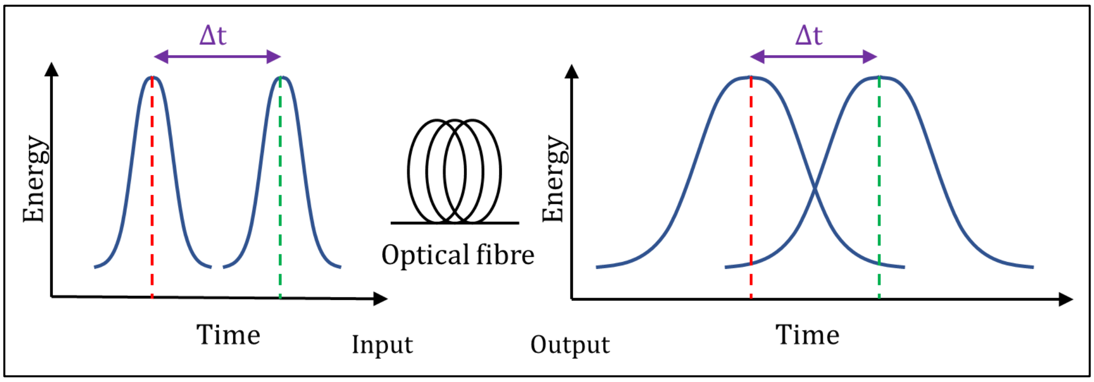

Figure 2.3. Effect of dispersion

Dispersion is caused by three key reasons [15], [17]:

(1) Different propagation paths for different rays, each with different propagation time. In mode propagation, each mode has a velocity causing this effect, known as *intermodal dispersion*. Single-mode fibre (SMF), which allows only one mode or light path, lack this effect.

(2) Variation of the refractive index with the optical frequency causes shifts in velocity and propagation time, as optical sources emit a range of wavelengths. This is an intrinsic property of the material and is known as *material dispersion*.

(3) Variation between group velocity and optical frequency, even if the refractive indexes are independent of wavelength, causes *waveguide dispersion*.

2.2.3 Losses in optical fibre

There are different phenomena which cause losses in optical fibres which effectively attenuates the optical power of the propagating signal. These effects have different causes and can be classified as absorption and scattering. The first absorbs energy from the signal and the latter transfer energy from the propagating wave to another direction.

a) Material absorption

The first kind of material losses is due to the interaction of the lightwave with the core raw material. Intrinsic losses in silica, the most common core material, come from the interaction of a photon with an electron, exciting it to a higher energy level, which is known as ultraviolet absorption. Another interaction is between the electromagnetic field and the vibrating chemical bond between atoms which causes energy transfer to the latter, known as infrared absorption [18] and is proportional to $e^{\frac{1}{\lambda_{IR}}-\frac{1}{\lambda}}$.

The other kind of material losses are due to the presence of impurities such as metal ions or hydroxide ions (OH^-). These extrinsic losses are caused by the vibrational resonance of the impurities ions and produce peaks of absorption at specific wavelengths. These peaks are proportional to the concentration of these impurities.

b) Radiative losses

Scattering due to structural imperfections in the fibre, and fibre's bends and curves cause radiative losses. Large-scale bends cause the light ray to hit the core-cladding interface with an angle greater than the critical angle. Therefore, the light is no longer guided. This loss is exponentially proportional to the bend radius.

The scattering effects are divided into linear, Rayleigh and Mie, and non-linear, Raman and Brillouin. In the commercial optical band, the most significant of these is the Rayleigh scattering which is proportional to λ^{-4}. See

Appendix A for details on these effects.

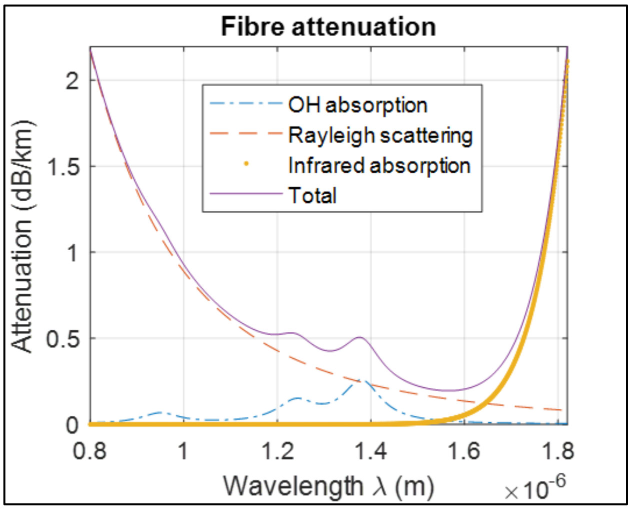

Figure 2.4. Single mode fibre attenuation profile

The telecommunications optical wavelength bands range from 1260 nm to 1625 nm and its major contributors for optical loss are Rayleigh scattering, Infrared absorption and extrinsic material absorption due to the OH^-. Figure 2.4 shows the loss profile of an SMF. See Appendix B or these calculations.

2.3 Multi-core optical fibre characteristics

As demonstrated in Figure 2.1, an optical fibre consists of a core material, commonly fused silica, surrounded by a cladding material. An MCF consists of more than one core inside of the same cladding. Each core is a waveguide with similar features as outlined in section 2.2, but MCFs have other properties. Figure 2.5 shows cross sections of different core lattices, where the cores are in blue and the cladding are in white.

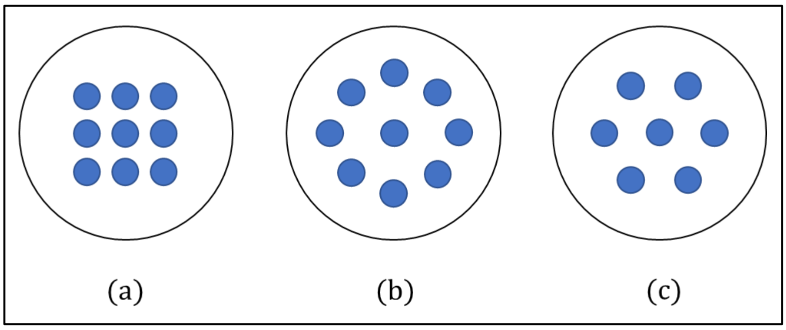

Figure 2.5. Different multi-core fibre cross sections: (a) rectangular, (b) circular and (c) hexagonal

2.3.1 Spatial division multiplexing

The concept of Spatial-division multiplexing (SDM) in optical fibres dates back to 1979 [19]. The new fibre technologies for high-capacity communications take advantage of SDM in high-performance MCFs, along with few-mode fibres (FMFs) and multi-core few-mode fibres (MC-FMFs) [20]. For instance, over 10 Peta-bit/s transmission has been demonstrated using 19-core MC-FMF with 6 modes, using SDM and wavelength-division multiplexing (WDM) [21].

The relation between capacity and the number of cores is inferred directly, as data transmission travels parallel along each core. Nevertheless, it is important to present the factor which affects the fibre's capacity. Equation 2.6 presents this relation, where C is the capacity, B is the effective transmission bandwidth, SE is the spectral efficiency, and N_{ch} is the number of spatial information channels. As detailed in [20], using values $B = 10THz, SE = 5{\sim}10\frac{bits}{s}Hz^{-1}$, and $N_{ch} = 2$, the theorical capacity is between 100 and 200 $Tbit/s$ per standard single-core single-mode fibre (SC-SMF). While this SC-SMF capacity is approaching its limit, SDM is a potential technique to improve capacity by increasing the number of spatial channels.

$$C = B \times SE \times N_{ch} \qquad (2.6)$$

There are different techniques for SDM, like fibre bundles and multi-element fibre (MEF), each with different features. Figure 2.6 shows these different techniques cross sections and illustrates the advantage of MCF: a lower number of cores per unit of area, or core density. A lower core density means more spatial channels, effectively more data transmission, in less cross-section. An MCF uses one fibre for several spatial channels while a fibre bundle uses one per spatial channel, which is a drawback when routing. Additionally, as presented in the sections 2.3.3 and 2.3.4, the distance between cores is also related to two features in MCF.

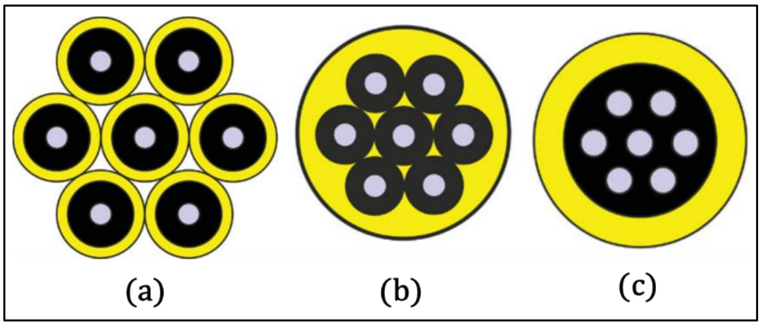

Figure 2.6. Different SDM techniques: (a) Fibre bundle, (b) Multi-element fibre and (c) Multi-core fibre

2.3.2 Core characteristics

The core of an MCF defines some of its properties. As mentioned in section 2.2.1, the core diameter defines the number of modes that a core conveys. The diameter of a core in single-mode MCF (SM-MCF) is about 9µm, allowing only one mode to propagate. A larger core diameter allows the propagation of more modes, typically 6-12 [20]. A core diameter of 16 µm -18 µm allows the transmission of 6 modes [21], [22].

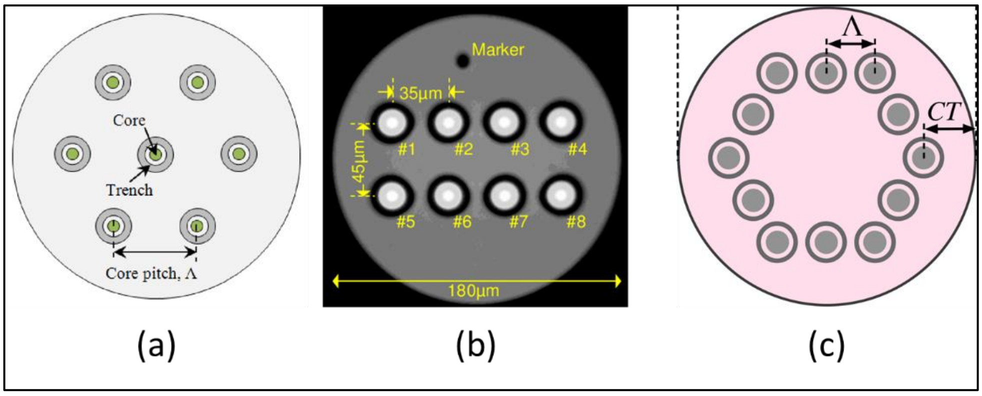

Figure 2.7. Different MCF core distribution demonstrating the core pitch [23]–[25]

The core pitch, which is the distance between cores such as in Figure 2.7, defines other properties of the MCF. Inter-core crosstalk (ICXT), which is analysed in the next section, depends on this parameter. Values of core pitch found in high capacity transmission experimental systems range from 35 µm to 50 µm [21], [24], [26], [27].

Another parameter of the MCF is the refractive index. A homogeneous MCF has the same refractive index for each core, while a heterogenous MCF has different ones, usually with no contiguous cores with the same refractive index, as depicted in Figure 2.8. Each of these types of MCF has different properties which are covered in the next two sections.

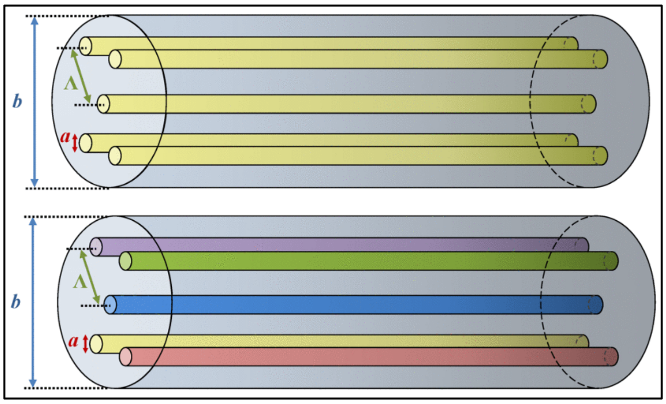

Figure 2.8. Homogeneous and heterogeneous MCF, with each colour representing a different refractive index [28]

2.3.3 Inter-core crosstalk

In MCF, ICXT is the coupling of the power from a signal in one or more cores into another core. This effect is graphically presented in Figure 2.9. Due to a high ICXT, two main limitations may exist: (1) achievable distance for high order modulation formats and (2) required optical signal-to-noise ration [26].

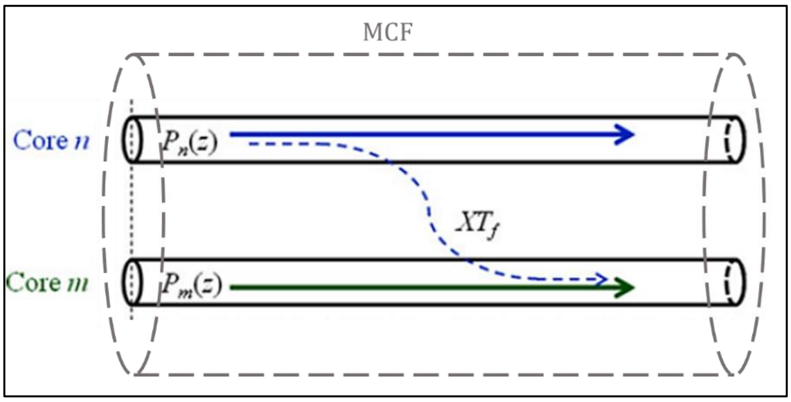

Figure 2.9. Inter-core crosstalk in MCF, modified from [29]

A mathematical representation of ICXT is the coupled-mode equation (*2.7*) [30], where $\boldsymbol{E}$ represent vector the electric fields of each core, $\boldsymbol{\beta_{eq}}$ represents the propagation constants diagonal matrix, including physical induced perturbations, and $\boldsymbol{\kappa}$ represents coupling coefficients matrix.

$$\frac{d\boldsymbol{E}}{dz} = -j\left(\boldsymbol{\beta_{eq}} + \boldsymbol{\kappa}\right)\boldsymbol{E} \qquad (2.7)$$

In [31] there is a mathematically derived discrete approximation of the total ICXT as the sum of the contributions in phase-matching points along the fibre. Also, in equation *2.8* a calculation is presented for the coupling coefficient between cores *m* and *n*, where R

is the bending radius, D_{mn} the distance between cores and γ the twist rate. This expression shows the trade-off between core distance and the coupling coefficient.

$$|K_{nm}| \cong \sqrt{\frac{\kappa}{\beta} \frac{R}{D_{mn}} \frac{2\pi}{\gamma}} \qquad (2.8)$$

ICXT reduction techniques aim to maintain core density, not to increase the core pitch. A trench-assisted MCF [23], [25] comprises of a material with a lower refractive index surrounding the core-cladding section, as shown in Figure 2.7 (a). A careful design of this MCF is necessary to suppress the long cut-off wavelength, especially in central cores. Another approach is to use heterogeneous MCF as it reduces the coupling between adjacent cores [23], [30]. However, this affects another parameter, which is presented in the next section.

Using coupled-mode theory and coupled-power theory [32], analysis of ICXT dynamics is presented in [31], [33], using the MCF parameters in Table 2.1. The calculated values in [31] for the mode-field diameter (MFD) and core coupling coefficient (K_{nm}) are 9.6 µm and 1.5x10^{-9} µm^{-1}, which finally gives the value of IC-XT of -42.9 dB. This ICXT computed value is in accordance with the average measured values.

Parameter	Value
Cladding refractive index, n_g	1.4445
Core-cladding index difference	0.42%
Bending radius, R	100 mm
Core pitch, D_{mn}	44.3 µm
Cladding diameter	160 µm
Outer diameter	281 µm
Length	28.3 km

Table 2.1. MCF parameters for ICXT calculation

2.3.4 Inter-core skew

In an MCF, each core conveys an optical signal, and the inter-core skew (IC-skew) is the difference between the time of travel, or propagation delay, of each signal in different cores, as depicted in Figure 2.10. Heterogeneous MCF has intrinsically non-zero IC-skew as each core's refractive index sets different velocities, thus resulting in different propagation delays.

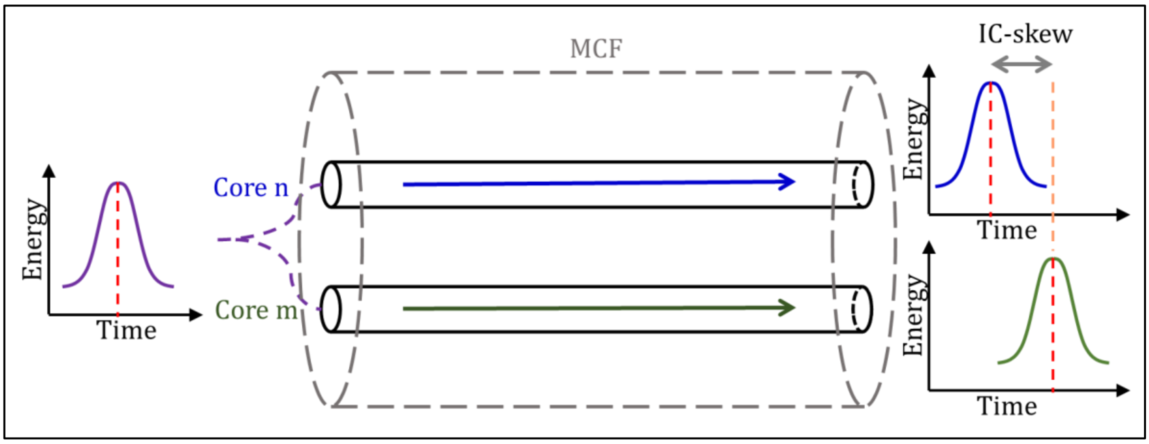

Figure 2.10. Inter-core skew.

For homogeneous MCF, as all cores have the same refractive index, the IC-skew should ideally be zero. However, experimental results [27], [31] show that not only is the IC-skew is in the order of nanoseconds, but also the IC-skew fluctuates in the order of picoseconds for fibre lengths of approximately 30 km and 50 km. Yet, a homogeneous MCF can achieve ultra-low ICXT values. In [34], the ICXT value is lower than -30 dB over 10,000 km. Low ICXT and low IC-skew make homogeneous MCF a suitable choice for optical communications.

Additionally, IC-skew is also affected by temperature, mechanical vibrations, and fibre imperfections. In [35], results indicate that longer fibres, which are prone to be affected by these factors, have higher dynamic IC-skew. These results also show that IC-skew fluctuations may correlated with the distance between cores, as this setup uses the central core as a reference point in different MCF layouts and shows higher IC-skew for the outer cores. Another experiment finds IC-skew fluctuations of less than 8ps for 28.3 km length 7-core homogeneous MCF [36]. A comparison between MCF and two different SMF is presented in [27], [36], showing higher IC-skew and its variation for the pair of SMF. This tendency can be applied also to fibre bundles and MEF, as the distance between cores is higher than in an MCF.

The importance of low IC-skew is the support of spatial superchannels (SSC), which are groups of same-wavelength subchannels transmitted on separate spatial modes but routed together. The benefits include sharing transmitter resources and less digital signal processing (DSP) load [37], using spatial dimension modulation formats and spatial encoding techniques [26], [31], which enable higher capacity transmissions. Therefore, it is necessary to understand the IC-skew and its dependence on environmental variables.

Chapter 3.

Thermal sensitivity of propagation delay and inter-core skew

Propagation delay and IC-skew in optical fibres can limit high-speed and precision-timing applications. Environmental variables affect these parameters. Thus, these effects are must be considered and compensated for if possible. This chapter covers the effects of temperature on these parameters, the technologies for reducing these parameters, and the techniques for thermal sensitivity measurement.

3.1 Temperature effect on the propagation delay

Chapter 2 presented an analysis of the structure of a conventional optical fibre and its light-guiding principle. For a particular core material with group refractive index n_g and length L, equation *3.1* provides the propagation delay.

$$\tau = \frac{n_g L}{c} \qquad (3.1)$$

The thermal coefficient delay (TCD) is the derivative of the propagation delay with respect to temperature and expressed per unit of fibre length, usually in kilometres. Consequently, its unit is usually ps/km-K. The derivate needs to consider the dependence of the refractive index and fibre length with temperature. From [38], [39], the equation for TCD is presented in the equation *3.2*.

$$TCD = \frac{1}{c}\left[n_g \frac{dL}{L\,dT} + \frac{dn_g}{dT} + \frac{dn_g}{d\sigma} E_f (K - k_f)\right] \qquad (3.2)$$

Each of this expression's terms represents a different effect. The first term represents the fibre's elongation change due to temperature. The second term represents the group refractive index change with temperature. Finally, the third represent the stress effect between the fibre and the jacket. As mentioned in [38], in standard SMF the last term is negligible, while if the SMF is surrounded by a protective coating, the last parameter is considered. For reference, TCD in a standard SMF is around 39 ps/km-K, which comes from the addition of 2 ps/km-K from the elongation change and 37 ps/km-k from the refractive index change [39], the first and second terms from equation *3.2*.

3.2 Temperature effect on the inter-core skew

As exposed in section 3.1, the propagation delay varies with temperature. In the case of the MCF, the temperature also affects the IC-skew, resulting in fluctuations in its value. Experiments focused on IC-skew measurement find that, without controlling the MCF temperature, these variations are less than a picosecond long [35], [36].

Furthermore, the experimental set-up in [27] uses a temperature controlled chamber to observe IC-skew variations in the different cores of a 7-core homogeneous MCF. The layout of this MCF is similar to Figure 2.7 (a), a centre core surrounded by six cores in a hexagonal distribution, with the IC-skew measurements relative to the centre core. The temperature range is 25° C to 45° C and the highest IC-skew values are 62 ps for heating and 42 ps for cooling for a fibre length of 53.7 km. Using these values, the thermal coefficient for IC-skew is 57.7 fs/km-K for heating and 39.1 fs/km-K for cooling.

3.3 Technologies for reduction of thermal sensitivity

3.3.1 Fibre coating

The most direct approach for alleviating any temperature effect is thermal coating. This approach consists of enclosing the optical fibre with a coating material which reduces any temperature effect. In [38] six different types of thermal coatings and a standard SMF are tested for thermal sensitivity for temperatures ranging from 5° C to 45° C. Referring to equation *3.2*, the fibre coatings work by changing the third term of the equation. The results show that the coated fibre from Furukawa has the best performance with a TCD of 3.7 ps/km-K.

Figure 3.1 shows different kinds of thermal coatings for SMF. From it, (a) is the standard SMF and (b) is the phase stabilised optical fibre (PSOF) coating which the best TCD. The main trade-off for the improvement in TCD is the increase in the outer diameter, which is 250 µm and 686 µm, for standard SMF and PSOF respectively. A higher outer diameter may be an impairment when scaling the number of optical fibres being routed.

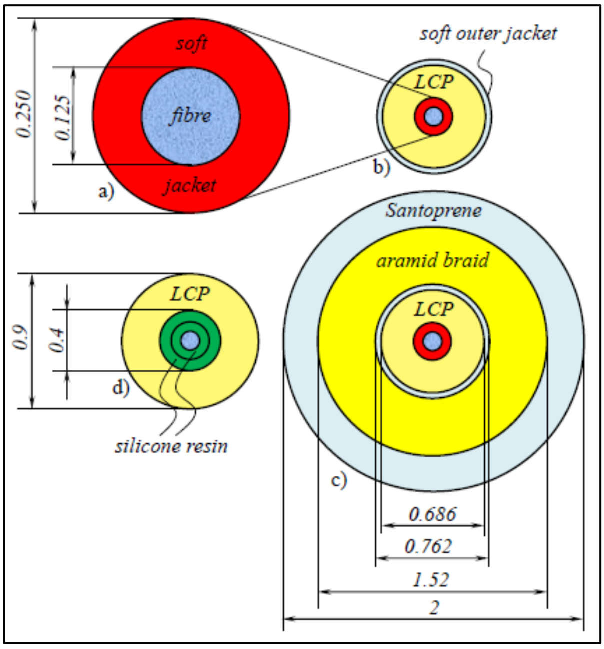

Figure 3.1. Different thermal coatings and their diameters: (a) standard SMF, (b) STFOC, (c) Non-Kink STFOC and (d) PSOF

3.3.2 Hollow-core Photonic Bandgap Fibre

Conceptually developed in the late 1990s, Hollow-core Photonic Bandgap Fibre (HC-PBGF) is a newer type of fibre which functions using a different physical principle than the dielectric optical fibre. As its name suggests, HC-PBGF guides light in a central hollow core surrounded by a cladding dielectric structure, such as silica glass.

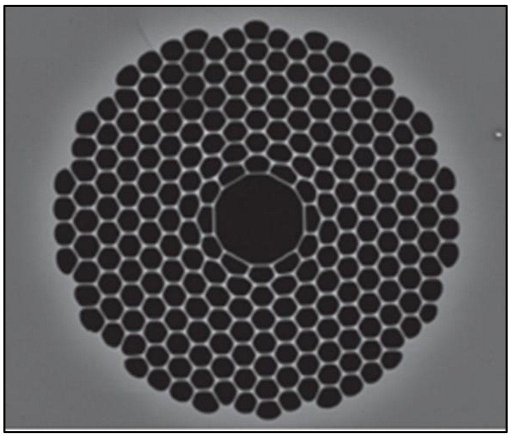

Figure 3.2. Hollow-core Photonic Bandgap Fibre cross-section [40]

The cladding is a holey dielectric periodic structure which creates a photonic bandgap (PBG) at specific wavelengths and angles of incidence. This bandgap is a frequency band of forbidden propagation for photons which are confined by and guided within the structure [40]. Figure 3.2 shows a cross-section of an HC-PBGF. The geometrical parameters of this structure and the refractive indexes of the holes, which are air's refractive index, and the structure all define the bandgap's properties.

Regarding TCD, experimental measurements show that its value is less than 2 ps/km-K, which comes from 1.42 ps/km-K from fibre elongation and approximately 0.13 ps/km-K from refractive index change, the first and second terms of equation *3.2* respectively [39]. Moreover, this low TCD comes with no effective increase in the outer diameter, which remains between 100 µm to 200 µm [40]. Among other advantages include ultralow non-linearity and strong resistance to radiation damage [41].

However, some parameters of the HC-PBGF are inferior compared to standard SMF. Fibre loss is significantly higher roughly 1.7 dB/km in a simulated 37-cell optimised HC-PBGF [40] which is an order of magnitude higher than standard SMF [42]. Unlike Rayleigh scattering, the surface scattering present in HC-PBGF scales proportionally to λ^{-3}. Another limitation is the usable bandwidth, which is defined by the bandgap. In [43], a 160 nm bandwidth for 3.5 dB/km loss and in [44], an 85 nm bandwidth for 3.3 dB/km loss, are demonstrated.

3.3.3 Zero sensitivity optical fibre

By using a combination of the previously presented technologies, a coated HC-PBGF with zero TCD is demonstrated in [41], with detailed mathematical expressions at a 1531 nm wavelength, 83 ps/nm-km dispersion, 10 nm to 20 nm bandwidth, 10 dB loss, and total outer diameter of 542 µm. The basic principle is to use the coating to increase the longitudinal expansion.

3.4 Thermal sensitivity measurement techniques

The experimental set-ups for thermal sensitivity to time parameters of optical fibres consist of two parallel measurements: time and temperature.

3.4.1 Correlation

The correlation technique is applied in [27], [31], [35], [36] for IC-skew fluctuations and its set-up is presented in Figure 3.3. This set-up requires a modulated optical signal, thus using a laser, a modulator and a pulse-pattern generator (PPG), which generates a 10Gb/s on-off keying (OOK), modulated signal a using 2^7-1 pseudo-random binary sequence (PRBS). This optical signal is amplified by an Erbium-doped fibre amplifier (EDFA) and filtered by a 1nm band-pass filter (BPF). Some differences between the mentioned experiments are the use of a no-return-zero (NRZ) modulation instead of an OOK and the use of a variable optical attenuator (VOA) after the BPF.

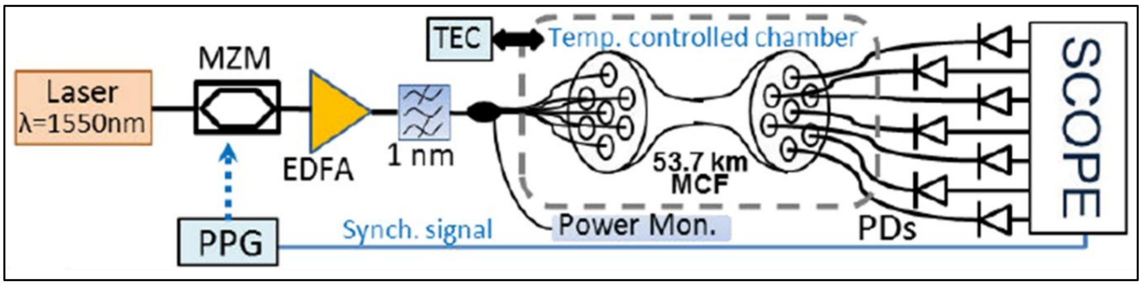

Figure 3.3. Experimental setup for IC-skew using correlation [27]

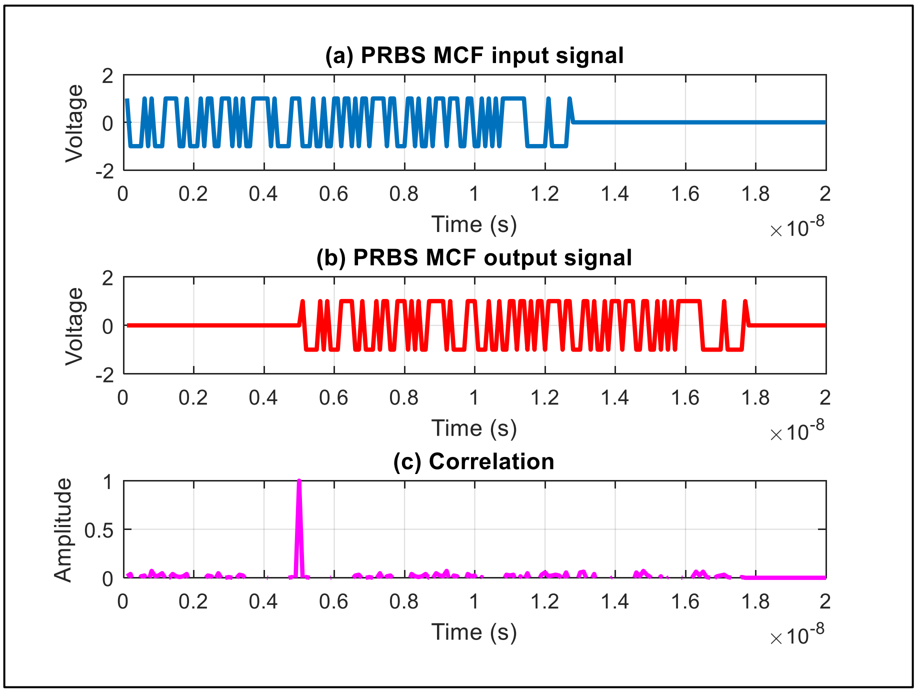

Figure 3.4. Correlation process: (a) Reference signal, (b) Delayed signal and (c) Correlation output

The modulated optical signal passes through a splitter to obtain several identical signals which are then sent to each core of the MCF. In the other end of the MCF, each core is connected to a photodetector (PD), which is connected to a channel of the oscilloscope with appropriate bandwidth and sampling considerations. Additionally, the PPG is connected to the oscilloscope as a reference point. The correlation process uses mathematical operations to compare signals and gives maxima when these are identical. In this setup, the oscilloscope performs a correlation between the reference and the PD output. The correlation peak's time difference from the reference demonstrates the delay. Figure 3.4 shows an example of a correlation between two time-delayed similar signals.

In [27] the temperature of the MCF is controlled by using a temperature controlled chamber. In this chamber, a sensor beside the fibre registers the temperature while heat pads increase the temperature. Additionally, this setup resolution is limited by the oscilloscope. In the referred experiment, the IC-skew variation is estimated by periodically cross-correlating 16 pairs of traces during a long period of time, similar to [36].

3.4.2 Optical delay interferometer

The interferometer technique uses a different principle from the correlation: an interference pattern of two optical signals gives information about the time delay between them. Figure 3.5 shows an example of this set-up, used in [39] for propagation delay fluctuation measurement.

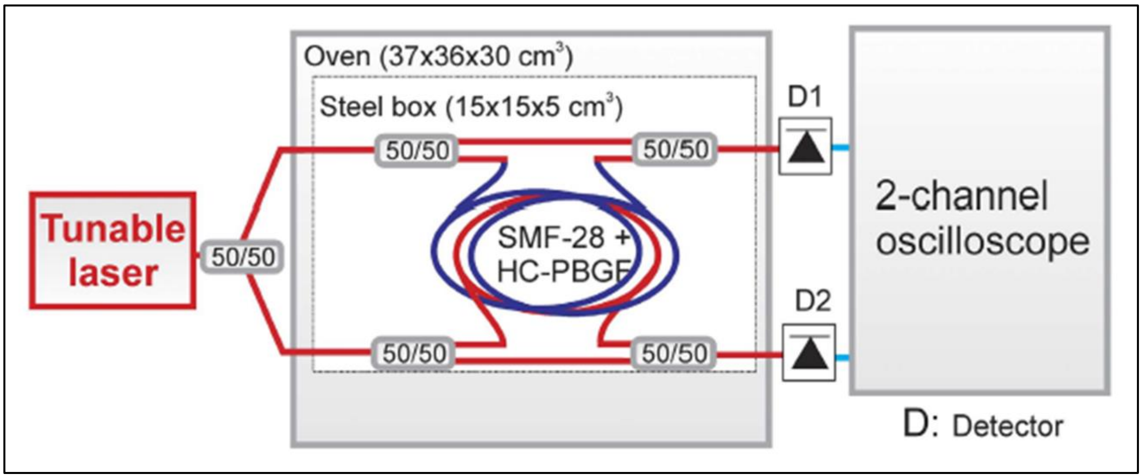

Figure 3.5. Optical delay interferometer set-up for propagation delay fluctuation measurement [39]

Figure 3.5 shows two interferometers. Therefore, it is relevant to outline the operation after the first 50/50 coupler. The interferometer uses a constant wave (CW) laser which, unlike in the previous set-up, does not require modulation. A 50/50 coupler splits the constant optical signal from the laser into two identical signals. While one signal travels through a short reference arm, the other signal is conveyed through a long spooled optical fibre. A second 50/50 coupler combines the signals from the reference arm and the spooled fibre, and this coupler’s output signal is converted to an electrical signal using a PD. An oscilloscope detects the output of the PD, which is the interference pattern.

The temperature of the couplers, the reference arm, and the spooled fibre are controlled, as these devices are placed inside of an oven. Due to the TCD, the signal transmitted through the spooled fibre is delayed by the signal from the reference arm. If the delay aligns in phase with the reference signal, the PD detects a peak of maximum optical power. While the delay increases, the phase difference increases and the PD detects a lower optical power until it reaches a minimum, when the delay is equal to a phase of π. After this point, the optical power detected by the PD starts to increase again.

One key advantage of the interferometer technique is its resolution, which is a factor that depends on the optical wavelength of the CW laser and the speed of light in the medium of the spooled fibre. In [39], using an HC-PBGF, the time resolution is around 2.59 fs for a 1550 nm wavelength.

Chapter 4.

Interferometer design and implementation

In Chapter 3, two techniques for time measurement in optical fibres were presented. While the correlation technique has been used for IC-skew measurement, the interferometer set-up offers better time resolution and less complexity, as it requires a CW optical signal instead of a modulated one. Therefore, the proposed experimental set-up is to use an interferometer to measure IC-skew fluctuations in an MCF and its temperature dependence.

4.1 Interferometer principle of operation

The interferometer requires, as mentioned in the previous chapter, a CW input signal. As the purpose of the set-up is to measure the time difference between the signals, the first stage is to produce two identical signals using a 50/50 splitter. The propagation through the upper arm of the interferometer produces a time delay Δτ. Both identical signals, now delayed in time one from the other, are combined in the second 50/50 coupler and then converted from optical power to an electrical current by the photodetector. The final stage is the visualisation of this electrical signal in an oscilloscope. The interferometer system, presented in Figure 4.1, may suffer from polarisation variations in its arms, which can cause a reduction in the amplitude of the optical waves and therefore in the power detected by the PD. A polarisation control mechanism can help reduce this effect, such as though a polarisation-maintaining fibre or a polarisation controller.

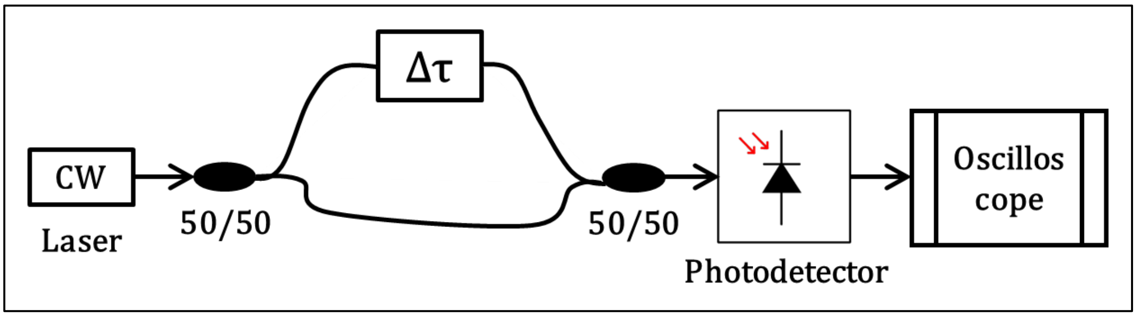

Figure 4.1. Interferometer schematic

For mathematical expressions of the output, the laser input is considered as an optical field of the form $E_{in(x,t)} = E_0 e^{-j(\omega t - kx)}$. This signal is divided in two and one is delayed in time, which is considered as a phase ϕ addition. The resulting field by adding both is given in equation *4.1*, which is the input of the photodetector.

$$E_{out(x,t)} = \frac{E_0}{2} e^{-j(\omega t - kx)} + \frac{E_0}{2} e^{-j(\omega t - kx + \phi)} \quad (4.1)$$

By arranging the terms of equation *4.1*, the equation *4.2* shows that $E_{out(x,t)}$ is effectively a modulation by the phase ϕ.

$$E_{out(x,t)} = \frac{E_0}{2}\left(1 + e^{-j\phi}\right) e^{-j(\omega t - kx)} \qquad (4.2)$$

The signal $E_{out(x,t)}$ is converted to an electrical signal by the photodetector. This device translates optical power into electrical current. Therefore, it is significant to understand the profile of the power, which is the square of the module of the field. Figure 4.2 depicts the profile and the periodicity of the optical power as a function of ϕ, and thus of the electrical signal detected by the oscilloscope: the period of the signal is 2π and goes from maximum to minimum every half period π. This figure uses $E_0 = 1$.

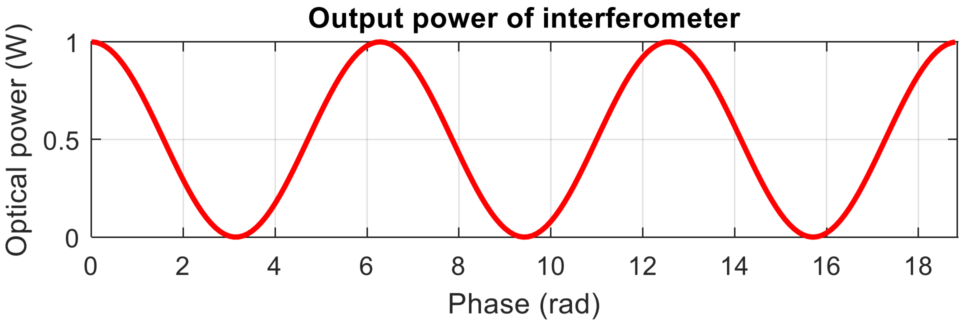

Figure 4.2. Output optical power of interferometer

In order to use this output for the computation of time delay, it is necessary to convert the phase information into the time domain. The reading from the scope changes from maximum to minimum in a phase equal to π, and this defines the resolution of the set-up: a phase change of π, which is a change in $\frac{\lambda}{2}$ of a wavelength. Therefore, the time value of each one of these changes Δτ is set by equation *4.3*, where v is the speed of light in the medium. Δτ is effectively the time resolution of the system.

$$\Delta\tau = \frac{\lambda}{2v} \qquad (4.3)$$

4.2 System design for inter-core skew measurement

4.2.1 System overview

The experimental set-up for IC-skew measurement adapts the interferometer operation and applies it towards measurement in an MCF. Figure 4.3 shows the proposed system design for IC-skew measurement in an 8-core MCF and each of its device.

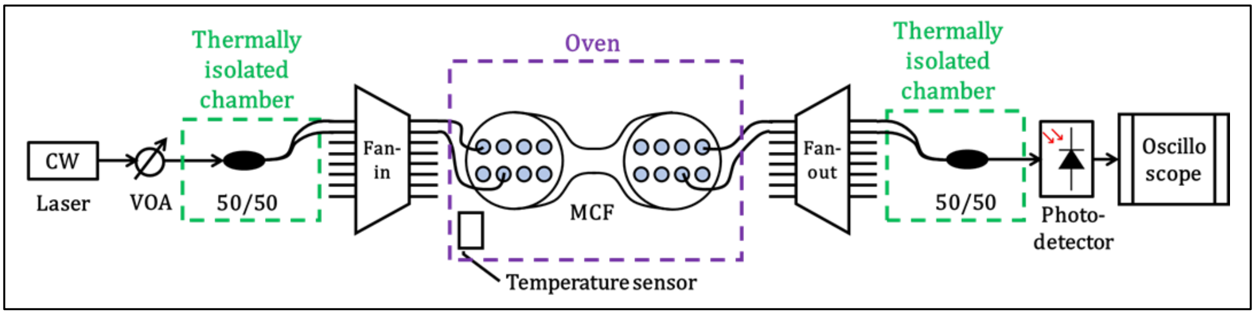

Figure 4.3. Proposed system design

The system uses a narrow-linewidth laser emitting an optical wavelength of 1550 nm. A VOA attenuates the optical CW signal from the laser in order to produce a suitable optical power. The attenuated optical signal is divided by a 50/50 optical coupler. For launching both identical optical signals to different fibre cores, a fan-in stage is used. An MCF conveys these signals in two different cores. Similar to the fan-in stage, a fan-out stage is used to transmit the signals from the MCF to the second 50/50 coupler. The output of the optical coupler is converted to an electrical signal by the PD. Finally, the oscilloscope detects the electrical signal from the PD.

As the aim of this setup is to measure the temperature dependency of the IC-skew, additional devices are in place to control the system's temperature. In Figure 4.3 the lines in green and purple represent these devices. A thermally isolated chamber, in green, helps to reduce the ambient temperature effects on the couplers. In purple, an oven is in place to heat the MCF and, inside of the oven, a temperature sensor registers its change.

The system uses the principle of operation outlined in section 4.1 to measure the variation in the time difference between the propagation delay of each arm of the interferometer, with one arm carrying the signal from one core and the other from a different core.

4.2.2 Components of the system

a) Laser and attenuator

The input of the system is a narrow-linewidth laser RIO ORION™ Laser Module. The wavelength of operation is 1550 nm, the output power is between 10 mW and 20 mW and maximum relative intensity noise (RIN) -140dB/Hz. After the laser, a VOA50-FC - SM VOA is in place to reduce the optical power, which operates at the same wavelength and has a maximum attenuation of 50 dB. The input of the interferometer is -13.6 dBm, effectively measured using an optical power meter.

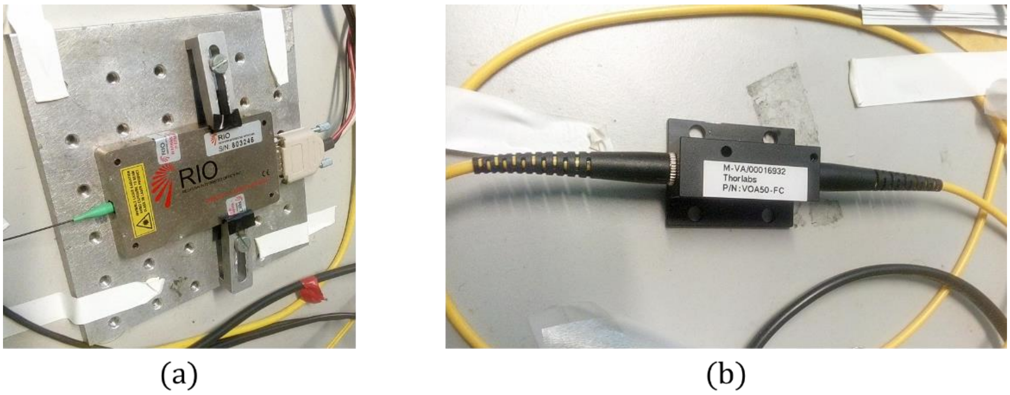

Figure 4.4. Images of (a) Laser and (b) Attenuator

b) Optical coupler

The interferometer implementation requires two 50/50 optical couplers. The optical couplers add a 5 dB loss. The first coupler divides the optical power into two identical signals, each signal having half of the intensity of the original signal. The second coupler combines the signal from each arm into a single signal with an intensity equal to the addition of its inputs.

Figure 4.5. Optical couplers

c) Fan-in and fan-out

Each stage allows to send and receive signals to and from the MCF and involves a total loss of approximately 4 dB. Additionally, as shown in Figure 4.3, the fan-in and fan-out stages are not thermally isolated, which may introduce noise and deviations to the readings.

Figure 4.6. Fan-in and fan-out

d) Multi-core fibre

The fibre used is an 8-core MCF, with a length of 1 km and a transmission loss between 0.220 dB/km and 0.303 dB/km. Figure 4.7 shows its cross-section and the core-to-core distance.

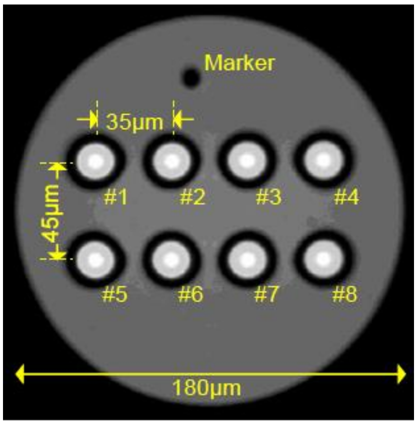

Figure 4.7. Cross-section of the MCF [24]

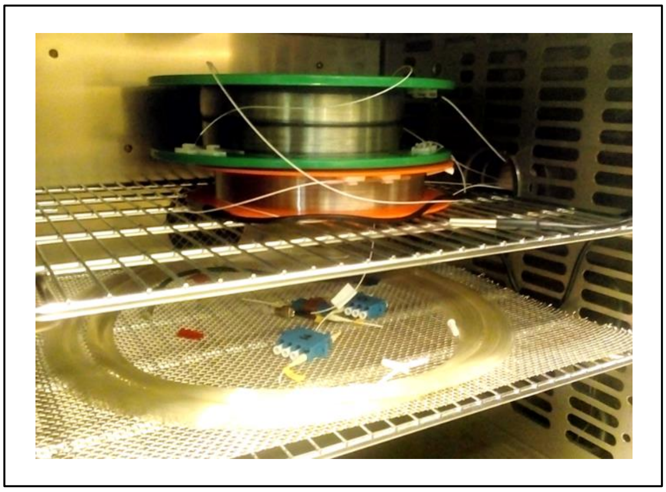

Figure 4.8. Multi-core optical fibre

e) Photodetector

The photodetector used is the Thorlabs DET01CFC, which is an InGaAs biased detector. The bias voltage is 9V and its bandwidth is 1.2GHz. The wavelength range of operation is 800nm to 1700nm.

Figure 4.9. Photodetector

f) Oscilloscope

The MDO 3012 Tektronik oscilloscope is used to detect the output of the PD with a bandwidth of 100 MHz. The signal of the PD is sampled at 50 S/s for 200s, providing 10000 samples. The output of the oscilloscope gives a resolution of 0.01 V, which is read by a PC via a USB connection and Tektronik software: TekVisa drivers and the Open Choice Desktop application.

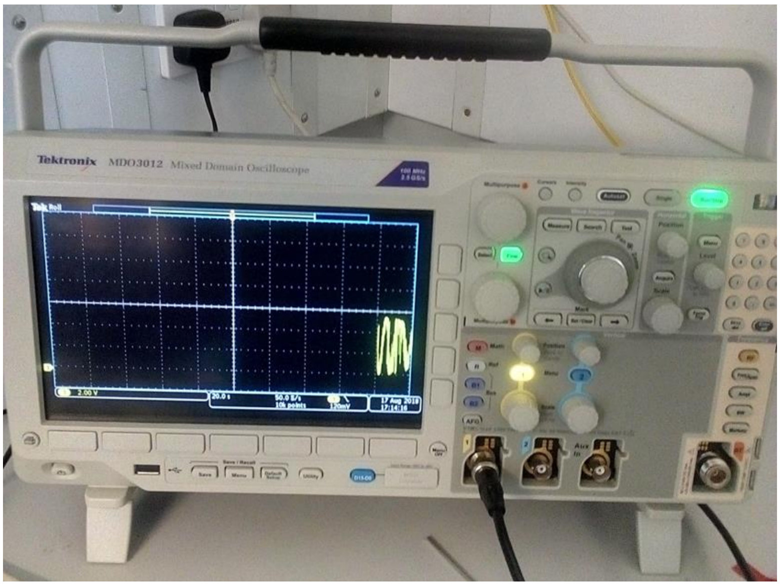

Figure 4.10. Oscilloscope

g) Oven

A Heraus 6000 series oven is used for the temperature increase of the MCF. The temperature increase in the oven's display is approximately 0.15° C/s. This is a reference point as the temperature sensor located inside of the oven records the actual temperature.

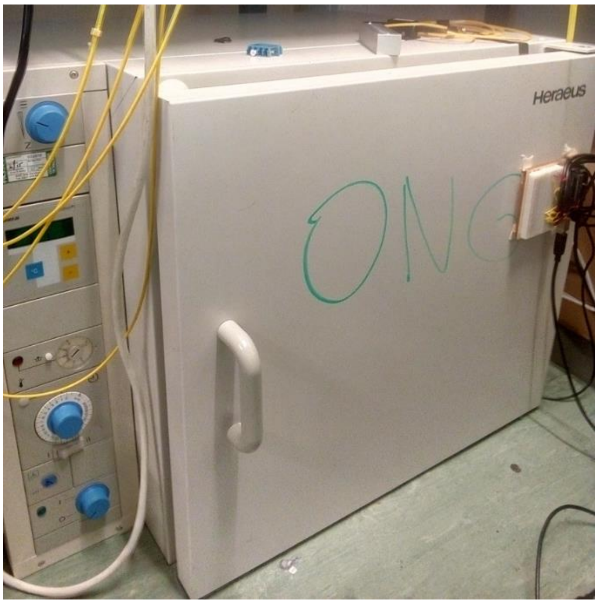

Figure 4.11. Oven

h) Temperature sensor

Three temperature sensors are placed inside the oven and electrically connected to an Arduino processor. The resolution of the temperature sensor is 0.01° C and the Arduino module is connected to a PC via USB. A MATLAB code reads the temperature of the three sensors at a sampling frequency of around 1 Hz.

i) Thermally isolated chamber

The thermally isolated chamber is a polystyrene box. The width of the walls is 5 cm and the box dimension is 1 m x 0.5 m x 0.7 m. The box has a removable top cover from the same material. The inside of the box is minimally affected by the environmental changes in temperature.

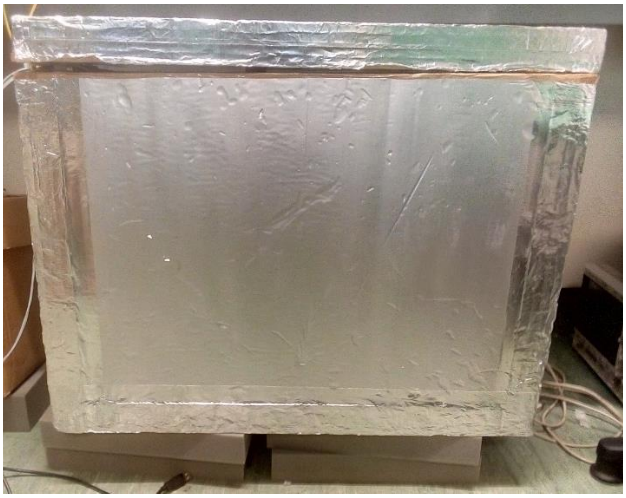

Figure 4.12. Thermally isolated chamber

4.3 Hardware implementation

The system was implemented in the CONNET laboratory on the 6th floor of the Roberts Building of the Department of Electronic & Electrical Engineering at the University College London. Mechanisms were implemented in an attempt to reduce external interference from ambient factors. As depicted in Figure 4.3, the optical couplers are placed inside of the thermally isolated chamber, and the MCF is located inside of the oven. However, the fan-in and fan-out stages are not located in either, which may introduce variations in the results due to ambient temperature changes.

Additionally, mechanical vibration is a factor that affects the IC-skew. Thus, the thermally isolated chamber and the fan-in and fan-out stages were placed over a damping foam to reduce it. The oven was located on the laboratory's floor, which may introduce a mechanical vibration effect.

The system was implemented by interconnecting all devices, as shown in Figure 4.3. The optical connections use FC connectors: laser output to VOA, VOA to the first coupler, and the second coupler to the PD. Also, LC connectors are used to connect to the fan-in and fan-out stages, so cables with an FC connector at one end and an LC connector at the other end are used to connect the couplers and the fan-in and fan-out. The PD output of the PD is an SMA female connector, and the input of the oscilloscope is a female BNC connector. Therefore, an SMA-BNC adapter is used for the connection between the PD and the oscilloscope.

4.4 Software implementation

The first experimental readings helped to understand the raw output of the interferometer, showing the system limitations and motivated enhancements, which are implemented via software.

The raw data files from the system are a voltage measurement from the PD and its time vector in a comma-separated value (CSV) file, and a temperature measurement from three sensors and its time vector in a CSV file. The software used for processing the files and plotting results is MATLAB, as it is suitable for operation with matrices.

Figure 4.13 shows a simplified flow diagram of the programme coded in MATLAB, including the main steps needed to obtain the results of IC-skew variations and its temperature dependence.

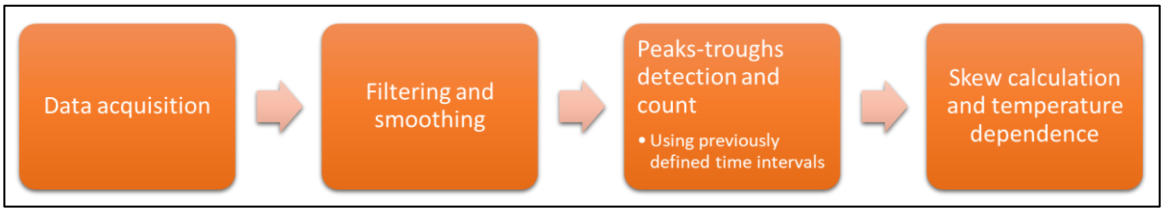

Figure 4.13. Flow diagram of the MATLAB program

Additionally, the temperature of the MCF is computed as the average of the three sensors' values. The temperature variation over time is required to obtain the MCF's IC-skew thermal dependence. The temperature sensor's time vector is interpolated and divided into steps which equal a temperature variation of 0.5° C. This divided time vector is used for counting the peaks and troughs of optical power over each time division.

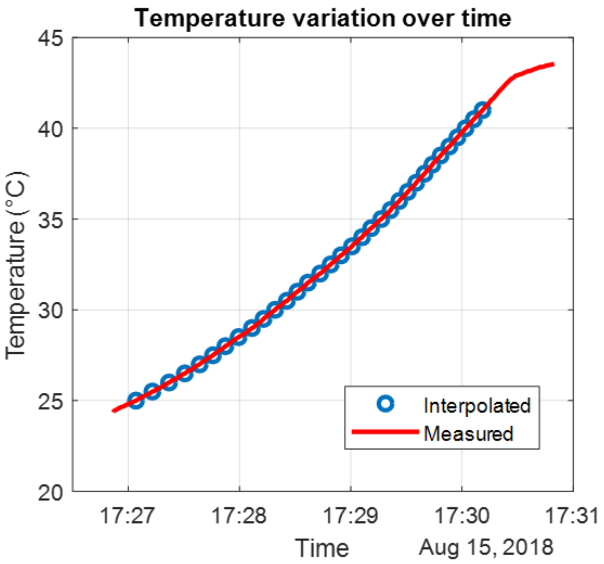

Figure 4.14. Example of temperature variation over time

The implemented MATLAB code is presented in Appendix C.

4.4.1 Filter and data smoothing

Due to different interference factors in the system, the electrical output of the PD needed processing in order to obtain readable maximum and minimum electrical currents without noise. Figure 4.15 shows the actual output of the photodiode in dashed lines and displays high-frequency noise for an experiment, which includes two cores of the MCF and its associated temperature increase. The signal processing parameters depend on the frequency information of the raw PD output signal, shown in Figure 4.16 (a). The signal has its higher power density in low frequencies with most of its energy being in frequencies below 2.5Hz. Also, there is a low frequency component and a DC component which are not desired, thus frequencies below 2.5 Hz are blocked. Therefore, a Butterworth BPF is used to reduce the higher and lower frequencies.

Additionally, a smoothing data process was used to reduce the ripples of the signal after the BPF. This process was considered after empirically analysing the output of the BPF to aid in the next stage of the software. The smoothing algorithm used a moving average window over the length of filtered data, and the window size is determined heuristically by the smooth data command. Figure 4.15 shows the output of the filtered and smoothed data, while Figure 4.16 (b) shows its frequency response. The smooth data process was tested with different sets of outputs and proved to work properly.

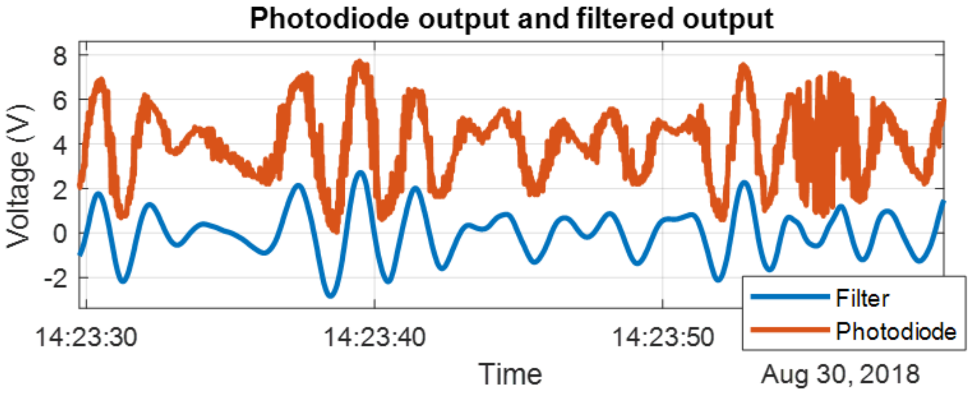

Figure 4.15. Example of the photodiode output and the filtered output

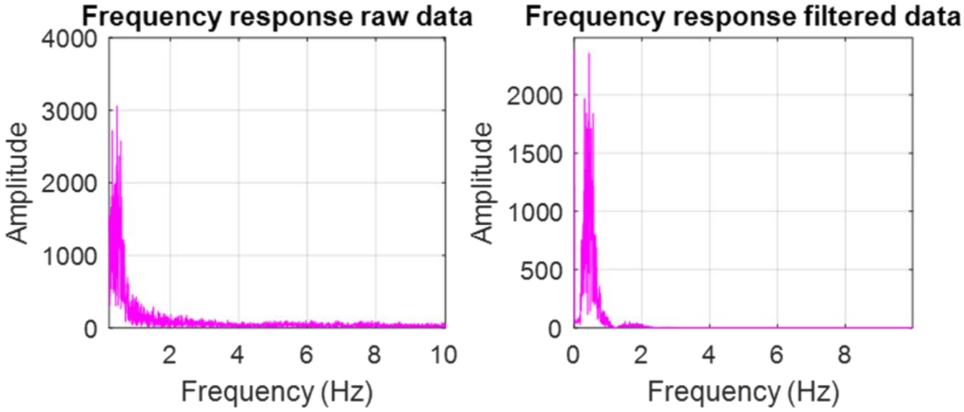

(a) (b)

Figure 4.16. Example of the frequency response of (a) Output of photodiode and (b) Filtered output

4.4.2 Peak-trough detection and count algorithm

The next step was to detect and count each peak and trough. This was achieved by first differentiating the data and then using the algorithm to detect peaks (which occur if the differentiated signal changes from positive to negative) and trough (which occur if the differentiated signal changes from negative to positive). Additionally, a threshold difference of 0.3 V between the value adjacent peak and trough is necessary. This value was found empirically. Figure 4.17 shows an example of this algorithm, which marks in red the peaks and in yellow the troughs.

As mentioned in section 4.1, the variations in the amplitude of the output of the PD might be caused by the variations in both arms' polarisation, in this case, in the MCF's two cores. Although this set-up has not implemented any polarization control mechanisms, it attempts to precisely detect the changes from maximum to minimum and vice versa, which is the relevant information for IC-skew variation calculations.

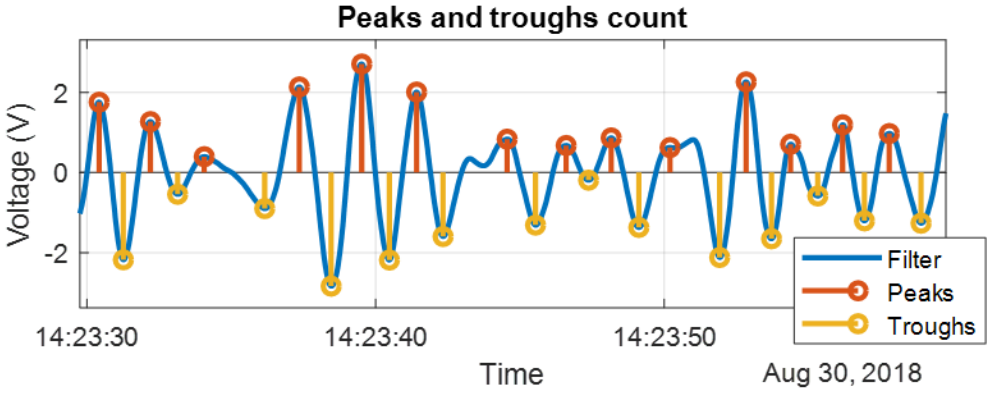

Figure 4.17. Examples of peaks and troughs detection

4.4.3 Skew calculation

As presented in section 4.1, a transition from a peak to a trough, or vice-versa, in optical power equals a Δτ in time. Hence, the peaks and troughs needed to be counted between time intervals. The time intervals were set by the divisions of the time vector from the previous section, which effectively gives a variation of 0.5° C.

The parameters of the system are presented in Table 4.1. Using these values as reference, the computed time resolution of the system is $\Delta\tau = 3.8\ fs$. Therefore, the IC-skew for each 0.5° C variation is the count of the peaks and troughs between the time interval multiplied by Δτ. The IC-skew variation with temperature was computed using the previous calculations.

System parameter	Value
Wavelength, λ	1550 nm
Group refractive index, n_g	1.47
Speed of light, c	299792458 m/s

Table 4.1. Parameters of the system

Chapter 5.

Results and discussion

An 8-core MCF with the characteristics presented in section 4.2.2 is used for the experiments on IC-skew variation. The core numbers correspond to the numbered layout of Figure 4.7. Each of the measurements was performed using the whole system: the hardware implementation of the interferometer and the software implementation for the signal processing and IC-skew calculation as outlined in the previous section.

5.1 Non-thermally induced inter-core skew variations

As part of the analysis of the accuracy of the system, seven IC-skew variation measurements were taken in the CONNET laboratory under regular conditions with the MCF placed in the oven but without any temperature increase and with the oven door closed. The chosen cores were core 1 and core 3, as these cores are neither the closest nor the furthest.

Figure 5.1 shows an example of an output of the system under the mentioned conditions. The filtered signal from only environmental noise represents around the 10% of the PD signal, which means that the filter allows this amount of noise to pass.

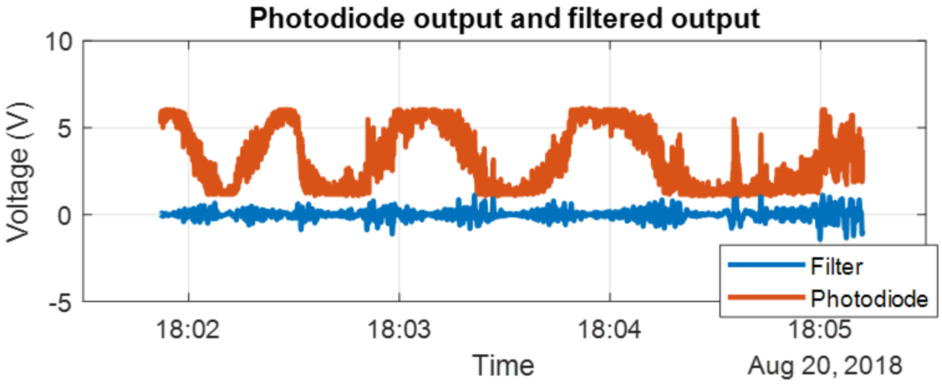

Figure 5.1. Peaks and troughs detection with no temperature variation

5.2 Thermally induced inter-core skew variations

The following measurements of inter-core skew variations are measured relative to core 1. The cores were changed to check the effect of relative distance between cores: moderate separate cores, adjacent cores and highly separate cores. Additionally, for each measurement, a first polynomial approximation for the variation of IC-skew against temperature was calculated, which led to equation *5.1*. The linear term, p_1, is the thermal coefficient in fs/K-km. An example of this approximation is shown in Figure 5.2.

$$p_{(x)} = p_1 x + p_2 \tag{5.1}$$

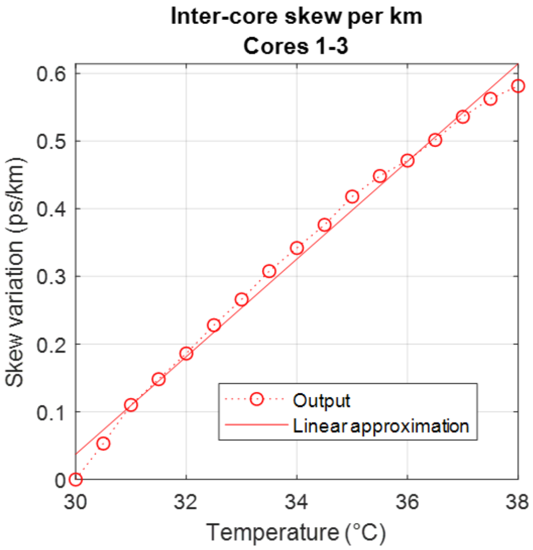

Figure 5.2. First polynomial approximation

Additionally, a statistical analysis of seven measurements of the thermal coefficient under similar conditions was completed for a fixed pair of cores. The results are presented in Figure 5.3, which also shows a Gaussian fit and its mean and variance values. This Gaussian fit has a low variance, however other measurements indicates higher values. The calculated value of the IC-skew is the mean of these measurements excluding the outliers.

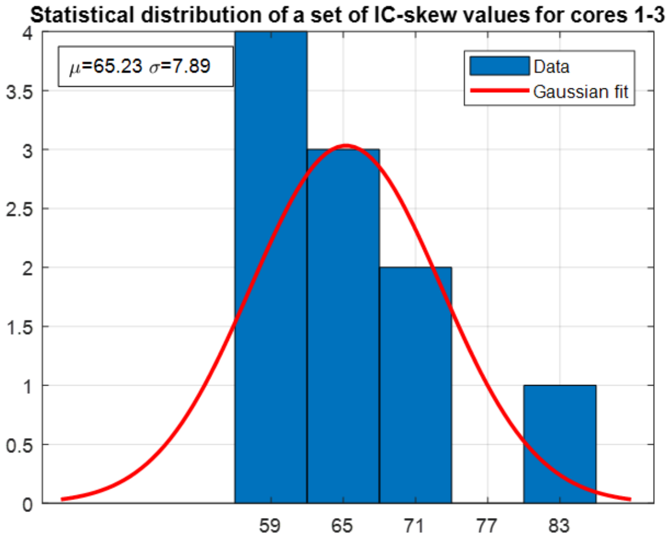

Figure 5.3. Statistical analysis of output

5.2.1 Moderate separate cores

Figure 5.4 demonstrates the results of four measurements using cores 1 and 3. The measurements start at different temperatures, but the thermal coefficients show consistent values, after excluding the highest value. The average of the calculated thermal coefficients, denoted as κ_{th}, is 63.40 fs/K-km.

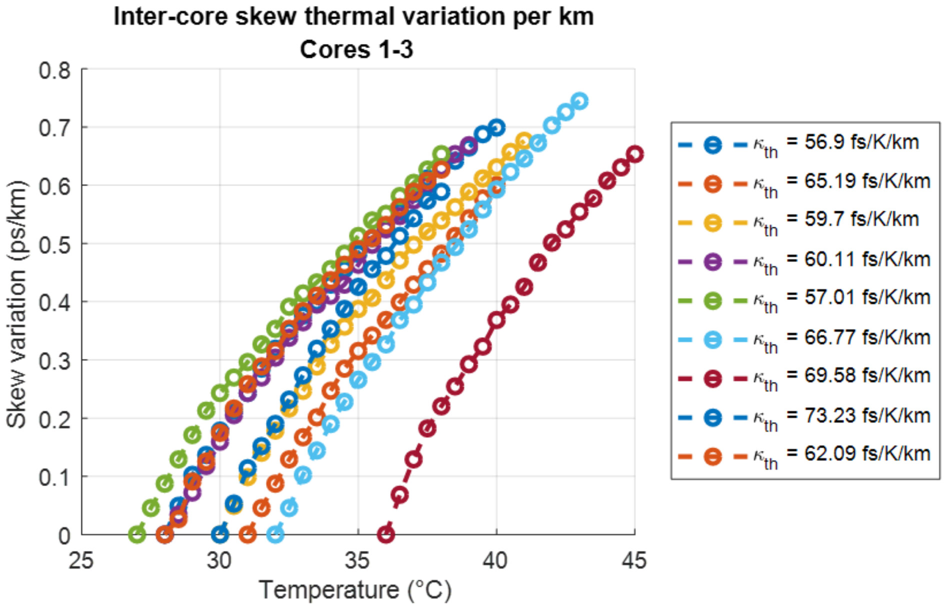

Figure 5.4. Inter-core skew thermal variation for cores 1 and 3

5.2.2 Adjacent cores

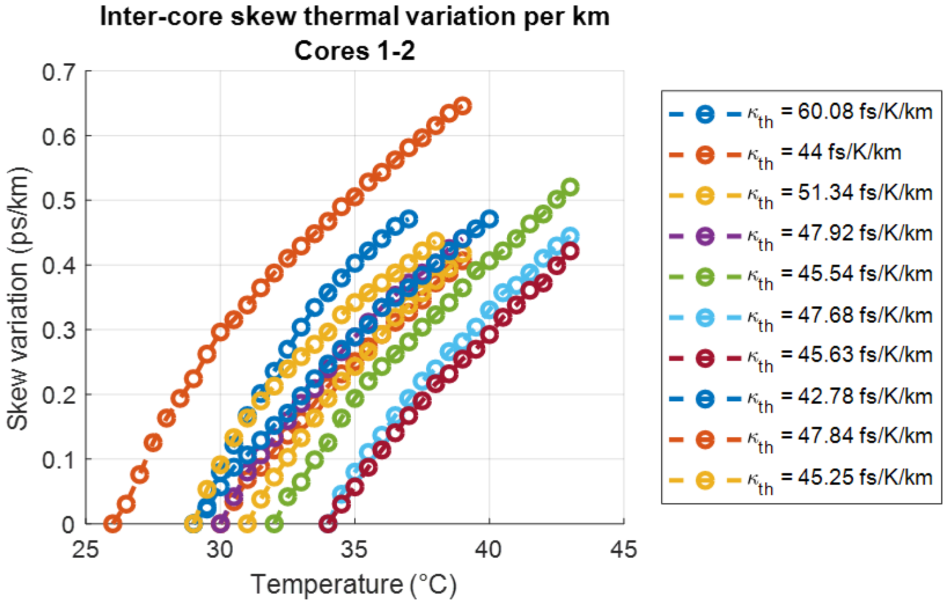

Figure 5.5. Inter-core skew thermal variation for cores 1 and 2

Figure 5.5 shows the results of four measurements using cores 1 and 2, which are adjacent cores. The measurements start at different temperatures, but the thermal coefficients again show consistent values. The average of the calculated thermal coefficients of each run is 46.44 fs/K-km.

5.2.3 Highly separate cores

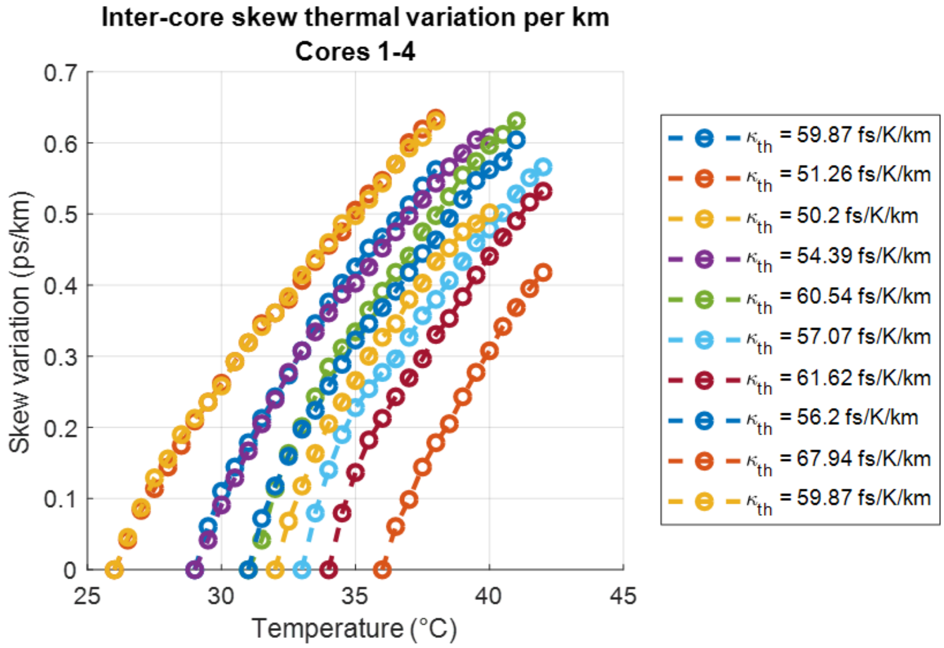

Figure 5.6. Inter-core skew thermal variation for cores 1 and 4

Figure 5.6 shows the results of four measurements using cores 1 and 4, which are both outer cores and have the largest distance between them. The measurements start at different temperatures and all the thermal coefficients show consistent values. The average of the calculated thermal coefficients is 57.90 fs/K-km.

5.3 Discussion and analysis

The values discussed in the previous section present a consistent measurement for IC-skew variations with temperature for an MCF. As presented in the previous section, these values have a 10% variation due to external interference when the MCF temperature was not altered.

In [27], the results show an IC-skew variation ranging from -8ps and 62ps for a 53.7 km and a temperature increase from 25° C to 45° C for heating. Using these values and equation 5.2, the maximum and minimum thermal coefficients are 57.73 fs/K-km and 7.45 fs/K-km respectively. The MCF used is a 7-core fibre with a hexagonal core layout and the measurements used the central core as a reference point. The distance between the central core and the outer cores is 44.2 µm.

$$\kappa_{thermal} = \frac{\Delta IC\ skew}{\Delta T \cdot L} \tag{5.2}$$

Despite the different layout between the MCFs, the maximum values of the IC-skew thermal coefficients for both fibres are comparable. Its maximum and minimum values are presented in Table 5.1. The IC-skew measured in [27] uses the central core as a reference point, and therefore the distance between cores is the same. However, the variation between the maximum and minimum is approximately 50 fs/K-km.

	Fibre used in this setup	**Fibre used in** [27]
Maximum value	63.40 fs/K-km	57.73 fs/K-km
Minimum value	46.44 fs/K-km	7.45 fs/K-km

Table 5.1. Comparison between IC-skew thermal coefficients for different fibres

Additionally, the results presented in section 5.2 suggest that there is a correlation between the IC-skew thermal coefficient and the distance between cores: the adjacent cores present the lowest IC-skew thermal coefficient. However, the pair of moderate separate cores have higher IC-skew thermal coefficients than the pair of highly separate cores.

as the distance between cores increases so does the IC-skew, and consequently, the thermal coefficient. This correlation is shown in Table 5.2. The first two values appear to increase linearly with the distance. However, this does not apply to the third value.

Distance between cores	**IC-skew thermal coefficient**
35 μm	46.44 fs/K-km
70 μm	63.40 fs/K-km
105 μm	57.90 fs/K-km

Table 5.2. Empirical correlation between thermal coefficient and distance between cores

Chapter 6.
Conclusion

6.1 Motivation

The arrival and steep growth of cloud services have triggered the development of a new type of data centre to cope with the higher data rates and capacity that these services demand. These hyper-scale data centres require higher speed interconnectivity and the current electronic devices present limitations for this capacity and speed demands.

In a data centre, regardless of its scale, the temperature profile is not constant neither in time nor in space due to the computational devices which heat up and require a cooling system. Therefore, any technology which comes to support higher capacity and speed needs to consider the possible effects of temperature on its performance.

6.2 Multi-core fibre capacity

The MCF presents similar features and impairments as standard fibre, such as higher bandwidth and lower loss profile than its electronic counterparts. Moreover, links with data rates higher than 10 Pb/s have been implemented using MCF and its SDM capability. Therefore, MCF is a promising technology for implementing links using higher data rates.

However, due to the proximity of the cores, the MCF also has other effects that need to be accounted for, such as ICXT and IC-skew. These effects can limit the maximum achievable data rate of the MCF. For its use in a data centre environment, the thermal influence on these effects must be characterised and reduced if possible.

6.3 Thermal effects attenuation in optical fibres

Optical fibre temperature variation leads to changes in the optical core signal’s propagation time. This change, in turn, can also limit the data rate capacity of an optical fibre.

Technologies exist to reduce the thermal effects. For example, the thermal coating material reduces the effects of temperature changes in the optical fibre. Also, HC-PBGF, which guides light using a different physical principle, shows a promising low sensitivity to temperature variations. Neverthelesss, these improvements come with trade-offs.

The thermal coating increases the outer diameter and limits the core density. In HC-PBGF, the guiding principle shows a higher loss and more limited bandwidth. In addition, these technologies combine to produce a zero sensitivity fibre.

6.4 The thermal effect in inter-core skew

Previous studies have shown a relationship between temperature and the IC-skew variations in MCFs using the correlation between a split signal sent to different cores. In this study, a different technique is used to measure the IC-skew variations which offer an improvement in the time resolution.

An interferometer system computes, the correlation between temperature and IC-skew variations. From the results presented in Chapter 5, there is a direct increase in IC-skew with temperature, which is the thermal coefficient. This coefficient shows a fairly linear behaviour in the range tested, between 25° C and 45° C.

Another significant result is the empirical correlation between IC-skew variation and the distance between cores. Two adjacent cores have lower IC-skew variation with temperature. However, no conclusive correlation was demonstrated as the distance increases.

The experimental set-up used in this study is the first attempt to use the interferometer technique to measure IC-skew variations in an MCF and its dependence on temperature.

6.5 Future research

The effects of IC-skew variations in MCF can limit its capabilities. In this study, the effects of temperature on IC-skew was analysed. This effect, as presented in Chapter 5, adds a difference in the propagation delay.

In a data centre environment, with temperature varying by position and time, the characterisation of the effects of temperature in an MCF is also useful for clock distribution, as it can help identify which core has the lowest thermal coefficient and use it for this purpose.

Three areas of future exploration in this field are as follow:

- Complete characterisation of the temperature dependence in IC-skew, in order to allow for adding phase shifts and to have constant propagation delays in all cores;
- Analysis of the temperature effect on IC-skew on different MCF core layouts under the same conditions.
- Future data transmission experiments using MCF, which include sending a clock signal in one core and data in the remaining ones for distances comparable to data centre interconnects.

References

[1] A. Regalado, "Who Coined 'Cloud Computing'?," *Technology Review*, 2011. [Online]. Available: http://www.technologyreview.com/business/38987/. [Accessed: 10-Jul-2018].

[2] L. Wang *et al.*, "Cloud computing: A perspective study," *New Gener. Comput.*, vol. 28, no. 2, pp. 137–146, 2010.

[3] Systems Kerridge Commercial, "A History of Cloud Computing Timeline," *Industry Insigths*, 2016. [Online]. Available: https://blog.kerridgecs.com/a-history-of-cloud-computing-timeline. [Accessed: 11-Jul-2018].

[4] L. Columbus, "83% Of Enterprise Workloads Will Be In The Cloud By 2020," 2018. [Online]. Available: https://www.forbes.com/sites/louiscolumbus/2018/01/07/83-of-enterprise-workloads-will-be-in-the-cloud-by-2020. [Accessed: 13-Jul-2018].

[5] L. Barroso and U. Hölzle, "The Datacenter as a Computer," *Morgan Claypool Publ. (May 2009)*, vol. 24, p. 156, 2013.

[6] Ethernet Alliance, "2016 Ethernet Roadmap," p. 455, 2016.

[7] Cisco, "Cisco Global Cloud Index : Forecast and Methodology , 2014–2019," *White Pap.*, pp. 1–41, 2014.

[8] A. Singh *et al.*, "Jupiter Rising: A Decade of Clos Topologies and Centralized Control in Google's Datacenter Network," *Proc. 2015 ACM Conf. Spec. Interes. Gr. Data Commun.*, pp. 183–197, 2015.

[9] K. I. Sato, "Realization and Application of Large-scale Fast Optical Circuit Switch for Data Center Networking," *Eur. Conf. Opt. Commun. ECOC*, vol. 2017–Septe, no. 7, pp. 1–3, 2018.

[10] N. Farrington and A. Andreyev, "Facebook's data center network architecture," *Opt. Interconnects Conf.*, pp. 49–50, 2013.

[11] J. H. Ahn, N. Binkert, A. Davis, M. McLaren, and R. S. Schreiber, "HyperX: Topology, Routing, and Packaging of Efficient Large-Scale Networks," *Proc. Conf. High*

Perform. Comput. Networking, Storage Anal. - SC ’09, no. Section 4, p. 1, 2009.

[12] T. Ahmed, S. Rahman, M. Tornatore, K. Kim, and B. Mukherjee, “A survey on high-precision time synchronization techniques for optical datacenter networks and a zero-overhead microsecond-accuracy solution,” *Photonic Netw. Commun.*, vol. 36, no. 1, pp. 1–12, 2018.

[13] K. S. Lee, H. Wang, V. Shrivastav, and H. Weatherspoon, “Globally Synchronized Time via Datacenter Networks,” *Proc. 2016 Conf. ACM SIGCOMM 2016 Conf. - SIGCOMM ’16*, pp. 454–467, 2016.

[14] M. K. Patterson, “The Effect of Data Center Temperature on Energy Efficiency,” 2008.

[15] G. P. Agrawal, *Fiber-Optic Communication Systems: Fourth Edition*. 2011.

[16] C. Woodford, “Fiber optics,” 2018. [Online]. Available: https://www.explainthatstuff.com/fiberoptics.html.

[17] A. K. (Ajoy K. . Ghatak, *An introduction to fiber optics / Ajoy Ghatak and K. Thyagarajan.* 1998.

[18] Optiwave Systems Inc., “Fiber Loss Models,” *OptiFiber Tutorials*, 2014. [Online]. Available: https://optiwave.com/optifiber-manuals/optical-fiber-fiber-loss-models/. [Accessed: 05-Jul-2018].

[19] S. Inao, T. Sato, S. Sentsui, T. Kuroha, and Y. Nishimura, “Multicore optical fiber,” *Opt. Fiber Commun. Conf.*, p. WB1, 1979.

[20] D. J. Richardson, “New optical fibres for high-capacity optical communications,” *Philos. Trans. R. Soc. A*, vol. 374, no. 2062, p. 20140441, 2016.

[21] D. Soma, Y. Wakayama, S. Beppu, S. Sumita, and T. Tsuritani, “10 . 16 Peta-bit / s Dense SDM / WDM transmission over Low-DMD 6-Mode 19-Core Fibre across C + L Band,” *J. Light. Technol.*, vol. 36, no. 6, pp. 1362–1368, 2018.

[22] R. Ryf *et al.*, “Mode-division multiplexing over 96 km of few-mode fiber using coherent 6×6 MIMO processing,” *J. Light. Technol.*, vol. 30, no. 4, pp. 521–531, 2012.

[23] J. Tu, K. Saitoh, M. Koshiba, K. Takenaga, and S. Matsuo, “Design and analysis of large-effective-area heterogeneous trench-assisted multi-core fiber,” *Opt. Express*, vol. 20, no. 14, pp. 15157–15170, 2012.

[24] T. Hayashi *et al.*, “End-to-End Multi-Core Fibre Transmission Link Enabled by Silicon Photonics Transceiver with Grating Coupler Array,” *Eur. Conf. Opt. Commun. ECOC*, vol. 2017–Septe, no. September, pp. 1–3, 2018.

[25] F. Ye, J. Tu, K. Saitoh, and T. Morioka, “Simple analytical expression for crosstalk estimation in homogeneous trench-assisted multi-core fibers,” *Opt. Express*, vol. 22, no. 19, p. 23007, 2014.

[26] B. Puttnam *et al.*, “High Capacity Transmission Systems Using Homogeneous Multi-Core Fibers,” *J. Light. Technol.*, vol. 35, no. 6, pp. 1–1, 2017.

[27] B. J. Puttnam, G. Rademacher, R. S. Luís, J. Sakaguchi, Y. Awaji, and N. Wada, “Inter-Core Skew Measurements in Temperature Controlled Multi-Core Fiber,” pp. 22–24, 2018.

[28] I. Gasulla and J. Capmany, “Microwave photonics applications of multicore fibers,” *IEEE Photonics J.*, vol. 4, no. 3, pp. 877–888, 2012.

[29] K. Saitoh, “Multicore Fiber Technology,” *Opt. Fiber Commun. Conf.*, vol. 34, no. 1, p. Th4C.1, 2015.

[30] I. P. Kaminow, T. Li, and A. E. Willner, *Optical fiber telecommunications. VI*. Kidlington, Oxford : Academic Press is an imprint of Elsevier, 2013., 2013.

[31] R. S. Luis *et al.*, “Time and Modulation Frequency Dependence of Crosstalk in Homogeneous Multi-Core Fibers,” *J. Light. Technol.*, vol. 34, no. 2, pp. 441–447, 2016.

[32] M. Koshiba, K. Saitoh, K. Takenaga, and S. Matsuo, “Multi-core fiber design and analysis: coupled-mode theory and coupled-power theory,” *Opt. Express*, vol. 19, no. 26, p. B102, 2011.

[33] G. Rademacher, R. S. Luís, B. J. Puttnam, Y. Awaji, and N. Wada, “Crosstalk dynamics in multi-core fibers,” *Opt Express*, vol. 25, no. 10, p. 12020, 2017.

[34] T. Hayashi, T. Taru, O. Shimakawa, T. Sasaki, and E. Sasaoka, “Design and fabrication of ultra-low crosstalk and low-loss multi-core fiber,” *Opt. Express*, vol. 19, no. 17, p. 16576, 2011.

[35] G. M. Saridis, B. J. Puttnam, R. S. Luís, W. Klaus, Y. Awaji, and G. Zervas, “Dynamic Skew Measurements in 7, 19 and 22-core Multi Core Fibers,” *Optoelectron. Commun. Conf.*, pp. MC2-1, 2016.

[36] R. S. Luis, B. Puttnam, J. M. Mendinueta, W. Klaus, Y. Awaji, and N. Wada, “Comparing inter-core skew fluctuations in multi-core and single-core fibers,” *CLEO Sci. Innov.*, p. SM2L--5, 2015.

[37] M. D. Feuer *et al.*, “Joint Digital Signal Processing Receivers for Spatial Superchannels,” vol. 24, no. 21, pp. 1957–1960, 2012.

[38] M. Bousonville *et al.*, “New phase stable optical fiber,” *Beam Instrum. Work.*, pp. 101–103, 2012.

[39] R. Slavík *et al.*, “Ultralow thermal sensitivity of phase and propagation delay in hollow core optical fibres,” *Sci. Rep.*, vol. 5, no. 1, p. 15447, Dec. 2015.

[40] F. Poletti, M. N. Petrovich, and D. J. Richardson, “Hollow-core photonic bandgap fibers: technology and applications,” *Nanophotonics*, vol. 2, no. 5–6, pp. 315–340, 2013.

[41] E. N. Fokoua, M. N. Petrovich, T. Bradley, F. Poletti, D. J. Richardson, and R. Slavík, “How to make the propagation time through an optical fiber fully insensitive to temperature variations,” *Optica*, vol. 4, no. 6, p. 659, 2017.

[42] C. Incorporated, “Corning ® SMF- 28 ® Ultra Optical Fiber,” no. November, 2014.

[43] N. V Wheeler *et al.*, “Wide-bandwidth, low-loss, 19-cell hollow core photonic band gap fiber and its potential for low latency data transmission,” vol. 1, pp. 19–21, 2012.

[44] Y. Jung *et al.*, “First Demonstration of a Broadband 37-cell Hollow Core Photonic Bandgap Fiber and Its Application to High Capacity Mode Division Multiplexing,” *Opt. Fiber Commun. Conf. Fiber Opt. Eng. Conf. 2013*, p. PDP5A.3, 2013.

[45] Fosco Connect, “Optical fibre loss and attenuation,” 2010. [Online]. Available: https://www.fiberoptics4sale.com/blogs/archive-posts/95048006-optical-fiber-loss-and-attenuation. [Accessed: 07-Aug-2018].

[46] H. Murata, *Handbook of Optical Fibers and Cables, Second Edition*. Taylor & Francis, 1996.

Appendix A

Scattering in optical fibre

i) Rayleigh scattering

Rayleigh scattering results from the microvariations of the density of the core material, which subsequently causes a random variation of the refractive index and a redirection of the light. These microvariations are small compared to the light wavelength. The Rayleigh scattering is proportional to λ^{-4} and depends on the physical parameters of the core material [15].

ii) Mie scattering

The cause of Mie scattering is imperfections in the core material which their size is comparable to the wavelength. These imperfections can be core-cladding refractive index variations along the fibre length, impurities at the core-cladding interface or core-diameter fluctuations [45]. The reduction of these imperfections aids in mitigating its effects.

iii) Stimulated Raman scattering

In stimulated Raman scattering, due to the lattice structure of the core material, the photon interacts with its molecules. The result is a non-linear effect: a transfer of the photon energy, which leads to a photon with less energy, and an optical phonon, which is a microscopic vibrational state in which molecules move out of phase, and can move in forward and backward directions [15].

iv) Stimulated Brillouin scattering

Like Raman scattering, in stimulated Brillouin scattering, photons and molecules interact and produce a photon with less energy and an acoustic phonon. In this phonon's vibrational state, molecules move in phase, which can occur in one direction and is maximum in the backward direction.

Appendix B

Loss calculation

The OH ions absorption includes attenuation proportional to parts per million (ppm) impurities in the optical fibre. It uses three parameters: (1) loss due to 1 ppm of impurity (dB/km), (2) absorption peak (nm), which is the wavelength at which the loss peak occurs, and (3) a delta of wavelength (nm), which defines the width of the peak.

Radical	**Loss due to 1ppm α_{OH} (dB/km)**	**Wavelength λ_{OH} (nm)**	**Delta wavelength $\Delta\lambda_{OH}$ (nm)**
OH^{-}_{1}	1.0	950	50
OH^{-}_{2}	2.0	1240	50
OH^{-}_{3}	4.0	1380	50

Table B.6.1 OH radical values for loss calculation

The loss is calculated using the formula from [18] in equation *B.1*. The value of α_{OH} is modified by a scale of 0.061 to fit standard SMF values.

$$L = \frac{\alpha_{OH}}{1+\frac{(\lambda-\lambda_{OH})}{\Delta\lambda_{OH}}} \qquad (B.1)$$

The Rayleigh scattering is proportional to λ^{-4} and is calculated using the formula from [46] and presented in equation *B.2*, with $A = 0.78 \times 10^{-24}$, derived from the same reference.

$$L = \frac{\mathrm{A}}{\lambda^4} \qquad (B.2)$$

Infrared absorption is an exponential curve that is calculated using the formula from [18] and presented in equation *B.3*.

$$L = 7.81 \times e^{\frac{-48\times10^{-6}}{\lambda}} \qquad (B.3)$$

All three formulas added together provide the total attenuation profile in dB/km.

The following MATLAB code calculates and plots the total loss.

```
%Define the set of lambda in nm
close all;
lambda = 800:1:1820;
lambda = lambda.*1e-9;
```

```
OH = [1.0 2.0 4.0; %Peak attenuation
    950e-9 1240e-9 1380e-9; %Wavelenth of absorption peak
    50e-9 50e-9 50e-9]; % Delta of peak absorption

OH(1,:) = OH(1,:).*0.61e-1;

att_OH = zeros(1,length(lambda));
att_rayleigh = zeros(1,length(lambda));
att_infrared = zeros(1,length(lambda));

%OH absorption calculation
for i=1:1:length(OH)
    for k=1:1:length(lambda)
        att_OH(k) = att_OH(k)+OH(1,i)/(1+(lambda(k)-
OH(2,i))^2/OH(3,i)^2);
    end
end

%Rayleigh scattering and infrared absorption calculation
for i=1:1:length(lambda)
    att_rayleigh(i) = 8.88e-25/(lambda(i))^4;
    att_infrared(i) = 7.81e11*exp(-48.48e-6/lambda(i));
end

att_total = att_OH + att_rayleigh + att_infrared;

figure;plot(lambda,att_OH,'-.',lambda,att_rayleigh,'--
',lambda,att_infrared...
    ,'.',lambda,att_total);grid('on');legend('OH absorption',...
    'Rayleigh scattering','Infrared absorption','Total');
title('Fibre attenuation');
xlabel('Wavelength \lambda (m)');ylabel('Attenuation (dB/km)');
axis([lambda(1) lambda(length(lambda-1)) 0 inf]);
```

Appendix C

MATLAB software implementation

This section contains two sets of codes: first, the code used for the system, and second, the code used for calculating and plotting the thermal coefficient.

i) Software implementation

```
%Read files with the name "readingsXXX_PD.csv" and "readingsXXX_temp.csv
%to get the variation of oscilloscope output and temperature over time.
%Also it reads the file "temperature.txt" which should have the initial
%temperature reading from the sensor.
%The resolution of the oscilloscope clock (initial time of the experiment
%is registered in hh:mm:ss) and temperature sensor clock resolution is
%0.0001s (initial time has a resolution of 0.01s) and its frequency is
%around 1Hz. The difference in initial times leads to an interpolation to
%get exact times.
%The sensitivity registered of the temperature sensor is 0.01°C.

clear;
close all;

%Read the files with data
file = 'readings133';
run = str2double(file(9:11));
PD_file = strcat(file,'_PD.csv');
temp_file  = strcat(file,'_temp.csv');

%Sampling period and frequency from oscilloscope
ts = xlsread(PD_file,'B2:B2');
fs = 1/ts;

%Read oscilloscope values
osc = xlsread(PD_file,'E:E');
osc = osc';

%Read experiment time
%The initial time is the time from the file minus 200s
[~,~,read_time] = xlsread(PD_file,'B17:B17');
read_time = char(read_time);
read_time = read_time(11:length(read_time));
init_time = datetime(read_time,'InputFormat','HH:mm:ss   d/MM/yy');
init_time = init_time - seconds(200);

%Read temperature values from file
temp_matrix = xlsread(temp_file,'A1:G314');
temp_matrix = temp_matrix';
temp_raw = (temp_matrix(4,:)+temp_matrix(6,:))./2;%+temp_matrix(7,:))./3;

%Read hour from the file temperatures.txt which needs to be updated when a
%new reading is taken.
temp_file=fopen('temperatures.txt');
temp_init_array = textscan(temp_file,'%s');
fclose(temp_file);
temp_init_time = datetime(strcat(string(temp_init_array{1}(run)),...
    read_time(11:length(read_time))),'InputFormat','HH:mm:ss.SS d/MM/yy');

%Matrixes for temperature and oscilloscope readings
%Each signal has its time vector
time_vector =init_time:seconds(ts):(init_time+seconds(ts*(length(osc)-1)));
temp_time = temp_init_time + seconds(temp_matrix(1,:));
```

```
%This value holds the temperature step variation: every temp_step the
%IC-skew is calculated
temp_step = 0.5;
%This sets up limits for the temperature readings and creates the
%temperature vector
temp_vector = ceil(min(temp_raw)):temp_step:(floor(max(temp_raw))-2);

%These steps delete the repeated values and calculate an interpolation of
%time vs temperature. The goal is to have a vector of times which marks the
%step increase of 0.5° C.
[temp, index] = unique(temp_raw);
temp_time_steps = interp1(temp,temp_time(index),temp_vector);

%Create Butterworth filter
osc_filter = osc;
fcutoff_h= 2.5; %In Hz
fcutoff_l= 0.25; %In Hz
[lpfb,lpfa] = butter(6,[fcutoff_l fcutoff_h].*2/fs,'bandpass')
%Apply Butterw;orth filter
osc_filter = filtfilt(lpfb,lpfa,osc_filter);
%Apply smoothing average algorithm to signal
osc_filter = smoothdata(osc_filter);

%Subplots
fig1=subplot(2,1,1);fig2=subplot(2,1,2);

%Plot the photodiode and filter output
figure
plot(fig1,time_vector,osc_filter,time_vector,osc,'Linewidth',2);
grid(fig1,'on');
xlabel(fig1,'Time');ylabel(fig1,'Voltage (V)');
title(fig1,'Photodiode output and filtered output');
legend(fig1,'Filter','Photodiode');

%These arrays hold the max and min (peaks and troughs respectively) for the
%hole oscilloscope data
max_v=[];
min_v=[];

%Initiate these arrays for ploting the peaks and troughs
osc_max = zeros(1,length(osc_filter));
osc_min = zeros(1,length(osc_filter));

%Derivate oscilloscope data to find the max and mins using a for loop
dev = diff(osc_filter);
for i=1:1:(length(dev)-1)
    if dev(i)>0 && dev(i+1)<=0
        %Slope change from positive to negative is a peak
        max_v = [max_v (i+1)];
        osc_max(i+1) = osc_filter(i+1);
    end
    if dev(i)<0 && dev(i+1)>=0
        %Slope change from positive to negative is a trough
        min_v = [min_v (i+1)];
        osc_min(i+1) = osc_filter(i+1);
    end
end

%These loops analyse the data and delete the peaks that are too small to be
%considered
k = 1;
threshold = 0.3;
%This code does the first analysis for a pair of peak and trough
while k <= length(max_v)
    if abs(osc_filter(max_v(k)) - osc_filter(min_v(k))) < threshold
```

```
        osc_max(max_v(k)) = 0;
        osc_min(min_v(k)) = 0;
        max_v(k) = [];
        min_v(k) = [];
        k = k-1;
    end
    k = k+1;
    if k+1>length(max_v) || k>length(min_v)
          break;
    end
end
%There is a difference if the signal starts with a trough or a peak, as it
%sets the direction of the analysis for the slope in the other direction
k = 1;
if min_v(1)>max_v(1)
    %Signal stars with max and the analysis goes from the current trough to
    %the next peak
    while k <= (length(max_v)-1)
      if abs(osc_filter(max_v(k+1)) - osc_filter(min_v(k))) < threshold
          osc_max(max_v(k+1)) = 0;
          osc_min(min_v(k)) = 0;
          max_v(k+1) = [];
          min_v(k) = [];
          k = k-1;
      end
      k = k+1;
      if k+1>length(max_v) || k>length(min_v)
          break;
      end
    end
else
    %Signal starts with min and the analysis goes from the current peak to
    %the next trough
    while k <= (length(min_v)-1)
      if abs(osc_filter(max_v(k)) - osc_filter(min_v(k+1))) < threshold
          osc_max(max_v(k)) = 0;
          osc_min(min_v(k+1)) = 0;
          max_v(k) = [];
          min_v(k+1) = [];
          k = k-1;
      end
      k = k+1;
      if k>length(max_v) || k+1>length(min_v)
          break;
      end
    end
end

%Set initial values for tempererature range and step of temperature
k = 1;m = 1;

%Vector for counting peaks and troughs, and skew
count = zeros(1,length(temp_time_steps));

%for loop runs over the whole time and count the peaks and troughs over
%each time interval which is related to a temperature
for k=1:1:length(time_vector)
    if time_vector(k)>=temp_time_steps(1)
        if time_vector(k)>=temp_time_steps(m) && ...
            time_vector(k)<temp_time_steps(m+1)
            if osc_max(k)~=0 || osc_min(k)~=0
                count(m+1) = count(m+1)+1;
            end
        else
            m = m+1;
        end
    end
    if m>=length(temp_time_steps)
```

```
        break
    end
end

%Vector for counting skew
skew = zeros(1,length(temp_time_steps));

%Add the counts to have total skew
for k=2:1:length(skew)
    skew(k) = sum(count(1:k));
end

%We know that each transition from peak to trough is in time lamba*ng/2c
c = physconst('Lightspeed');
ng = 1.47;
lambda = 1550e-9;
fiber_km = 1; % in km
time_scale = 1e-12; %picoseconds

scale = lambda*ng/(2*c*time_scale*fiber_km);

%Plot the filter output with the result of the algorithm to find peaks and
%troughs
osc_max(osc_max==0)= NaN;
osc_min(osc_min==0)= NaN;
plot(fig2,time_vector,osc_filter,'Linewidth',2);grid(fig2,'on');
hold(fig2,'on');
stem(fig2,time_vector,osc_max,'Linewidth',2);
stem(fig2,time_vector,osc_min,'Linewidth',2);
hold(fig2,'off');legend(fig2,'Filter','Peaks','Troughs');
title(fig2,'Peaks and troughs count');
xlabel(fig2,'Time');ylabel(fig2,'Voltage (V)');

%Plot the temperature variation over time
plot(temp_time_steps,temp_vector,'o',temp_time,temp_raw,'r','LineWidth',2);
grid('on');xlabel('Time');ylabel('Temperature (°C)');
title('Temperature variation over time');
legend('Interpolated','Measured');

%Plot the inter-core skew with the time scale
figure
plot(temp_vector,skew.*scale,'ro:');lsline;
title({'Inter-core skew per km'; 'Cores 1-3'});grid('on');
xlabel('Temperature (°C)');ylabel('Skew variation (ps/km)');
legend('Output','Linear approximation');

%Plot fourier
figure
b1 = subplot(1,2,1);b2 = subplot(1,2,2);
%Frequency of output without filter and DC reduction
freq = (-fs/2):fs/length(osc):(fs/2-fs/length(osc));
plot(b1,freq,abs(fftshift(fft(osc-(max(osc)+min(osc))/2))),'m');
grid(b1,'on');title(b1,'Frequency response raw data');
ylabel(b1,'Amplitude');xlabel(b1,'Frequency (Hz)');
xlim(b1,[0 inf]);
%Frequency of output with filter and DC reduction
plot(b2,freq,abs(fftshift(fft(osc_filter-(max(osc_filter)+...
    min(osc_filter))/2))),'m');
grid(b2,'on');title(b2,'Frequency response filtered data');
ylabel(b2,'Amplitude');xlabel(b2,'Frequency (Hz)');
xlim(b2,[0 inf]);
```